SPECIAL RELAMPAGO-CACTI COLLECTION

SPECIAL PECAN COLLECTION

Low-Level Mesoscale and Cloud-Scale Interactions Promoting Deep Convection Initiation

JAMES N. MARQUIS,[a,b] ADAM C. VARBLE,[a] PAUL ROBINSON,[b] T. CONNOR NELSON,[b,c,d] AND KATJA FRIEDRICH[b]

[a] *Pacific Northwest National Laboratory, Richland, Washington*
[b] *University of Colorado, Boulder, Colorado*
[c] *Cooperative Institute for Research in the Atmosphere, Fort Collins, Colorado*
[d] *NOAA/NWS Operations Proving Ground, Kansas City, Missouri*

(Manuscript received 26 November 2020, in final form 3 May 2021)

ABSTRACT: Data from scanning radars, radiosondes, and vertical profilers deployed during three field campaigns are analyzed to study interactions between cloud-scale updrafts associated with initiating deep moist convection and the surrounding environment. Three cases are analyzed in which the radar networks permitted dual-Doppler wind retrievals in clear air preceding and during the onset of surface precipitation. These observations capture the evolution of (i) the mesoscale and boundary layer flow, and (ii) low-level updrafts associated with deep moist convection initiation (CI) events yielding sustained or short-lived precipitating storms. The elimination of convective inhibition did not distinguish between sustained and unsustained CI events, though the vertical distribution of convective available potential energy may have played a role. The clearest signal differentiating the initiation of sustained versus unsustained precipitating deep convection was the depth of the low-level horizontal wind convergence associated with the mesoscale flow feature triggering CI, a sharp surface wind shift boundary, or orographic upslope flow. The depth of the boundary layer relative to the height of the LFC failed to be a consistent indicator of CI potential. Widths of the earliest detectable low-level updrafts associated with sustained precipitating deep convection were ~3–5 km, larger than updrafts associated with surrounding boundary layer turbulence (~1–3 km wide). It is hypothesized that updrafts of this larger size are important for initiating cells to survive the destructive effects of buoyancy dilution via entrainment.

KEYWORDS: Convective storms; Convective-scale processes; Mesoscale processes; Storm environments; Radars/radar observations; Soundings

1. Introduction

Correctly representing moist convective processes is critical to accurately predicting regional and global weather and climate, and accompanying operational forecasting of near- and long-term hydrology and severe weather. Numerical simulations rely on a mix of cumulus, turbulence, microphysics, and planetary boundary layer parameterization schemes to represent the generation of shallow and deep moist updrafts and precipitation (e.g., Tiedtke 1989; Kain and Fritsch 1990; Kain 2004; Yano et al. 2004; Bretherton et al. 2004; Wagner and Graf 2010; Chikira and Sugiyama 2010; Derbyshire et al. 2011; Kim and Kang 2011). An important component of understanding all of these phenomena is determining how growing updrafts interact with the surrounding environment to initiate sustained deep moist convection.

Processes leading to the initiation of deep convection often entail a reduction or removal of convective inhibition (CIN) and vertical perturbation of air parcels to their level of free convection (LFC) to release convective available potential energy (CAPE). Elimination of CIN does not necessarily guarantee deep convection initiation because a reduction of in-cloud vertical momentum and positive buoyancy can occur from opposing vertical pressure gradient forces and entrainment of the surrounding air into the updraft (e.g., Rhea 1966; Ziegler and Rasmussen 1998; de Rooy et al. 2013; Morrison 2017; Peters et al. 2019). Organized mesoscale horizontal flow convergence frequently aids convection initiation processes by forcing low-level air parcels upward, locally reducing CIN, deepening boundary layer moisture below cloud base, and providing a focal area for moist updrafts to detrain into the overlying free troposphere, reducing the negative entrainment effect (Ziegler et al. 1997; Markowski and Richardson 2010; Moser and Lasher-Trapp 2017). Common mesoscale convergence features that trigger deep convection initiation (hereafter CI) arise from surface air mass or wind shift boundaries such as fronts, drylines, and cold pool gust fronts (e.g., Wilson and Schreiber 1986; Kingsmill 1995; Wilson and Megenhardt 1997; Ziegler and Rasmussen 1998; Lee et al. 2000; Arnott et al. 2006; Hirt et al. 2020); orographic circulations (e.g., Kottmeier et al. 2008; Demko et al. 2009;

Denotes content that is immediately available upon publication as open access.

Corresponding author: James N. Marquis, james.marquis@pnnl.gov

DOI: 10.1175/MWR-D-20-0391.1

Demko and Geerts 2010; Kirshbaum 2011; Kirshbaum et al. 2018; Mulholland et al. 2020); interactions with convective boundary layer (hereafter CBL) circulations (e.g., Wilson et al. 1992; Atkins et al. 1995; Peckham et al. 2004; Xue and Martin 2006); and horizontal heterogeneities of surface properties (e.g., Kang and Bryan 2011; Garcia-Carreras et al. 2011; Huang and Margulis 2013; Rieck et al. 2014).

A complete understanding of the specific controls on CI is limited partly by our inability to adequately observe the near-cloud environment. A variety of field studies, such as the Convection Initiation and Downdraft Experiment (Wilson et al. 1988), the International H_2O Project (Weckwerth et al. 2004), the Convective Storm Initiation Project (Browning et al. 2007), the Convective and Orographically-induced Precipitation Study (COPS; Wulfmeyer et al. 2008), and the Cumulus Photogrammetry In situ and Doppler Observations experiment (Damiani et al. 2008), aimed to map mesobeta- and mesogamma-scale kinematic and thermodynamic heterogeneity surrounding focal areas of CI. Superimposed surface mesoscale convergence, complex orography, and CBL circulations can yield significant sub-10-km-scale variation among environmental CAPE, CIN, moisture, and wind shear fields in the area immediately surrounding forecasted CI locations (e.g., Weckwerth et al. 1996; Markowski and Richardson 2007; Ziegler et al. 2007; Kalthoff et al. 2009; Behrendt et al. 2011; Khodayar et al. 2010, 2013; Nelson et al. 2021).

In addition to uncertainties regarding the measurement of the near-cloud environment, many fundamental processes regarding how cloud-scale updrafts interact with their environment during CI are not well understood. Recent theoretical and cloud-scale LES studies demonstrate that convective cloudy updrafts are composed of $O(1)$-km-wide ascending buoyant thermals (e.g., Zhao and Austin 2005; Houston and Niyogi 2007; Kirshbaum 2011; Varble et al. 2014; Morrison 2016; Moser and Lasher-Trapp 2017). The size of a thermal may partly control the amount of buoyancy dilution within the cloud (Morrison 2017); thus, initial updraft width could be one factor governing CI. Numerical representation of updraft size and vertical mass flux is sensitive to the model grid resolution (e.g., Bryan et al. 2003; Varble et al. 2014; Varble et al. 2020; Hirt et al. 2020), as well as other physical parameterizations, limiting what can be ascertained about updraft-environment interactions using convection-allowing mesoscale models. A more complete understanding of CI requires synchronized observation of the near-cloud mesoscale environment and cloud-scale [$O(100)$ m] depiction of three-dimensional (3D) flow in and below deepening convective updrafts to validate theoretical and LES-based hypotheses. However, such observations are difficult to acquire owing to the need for fortuitously positioned scanning radars, as well as possible dangers associated with penetrating potentially intense deep midlatitude convection with typical aircraft (e.g., Musil et al. 1991; Rosenfeld et al. 2006; Honomichl et al. 2013).

In this study, we focus on understanding warm season midlatitude CI using observations from three cases collected during recent field campaigns: the Remote Sensing of Electrification, Lightning, and Mesoscale/Microscale Processes with Adaptive Ground Observations (RELAMPAGO; Nesbitt et al. 2021) project, the Cloud, Aerosol, and Complex Terrain Interactions (CACTI; Varble et al. 2021) project, and the Plains Elevated Convection At Night (PECAN; Geerts et al. 2017) experiment. These field campaigns deployed balloon radiosondes, scanning precipitation radars, and vertically profiling lidars and radiometers to detail the environments supporting CI. Three-dimensional dual-Doppler wind retrievals are conducted for all three cases, documenting flow structure in the boundary layer for several hours leading up to and during CI. These data allow estimation of the size, structure, and evolution of early convective updrafts in the context of the surrounding environmental thermodynamic conditions and mesoscale flow. Dual-Doppler wind observations surrounding CI are rare; thus, these analyses provide a unique opportunity to improve our understanding of complex multiscale convective processes.

Section 2 outlines the critical instrumentation deployed during the three CI missions examined in this study. Section 3 discusses the evolution of the boundary layer flow, mesoscale triggering mechanisms, and environmental profiles leading up to CI. Section 4 analyzes the evolution and intensity of the dual-Doppler-retrieved low-level convective updrafts at their earliest detectable stages. Last, sections 5 and 6 compare analyses across the three cases and synthesize conclusions.

2. Cases and datasets

A primary objective of the concurrent RELAMPAGO and CACTI projects was to observe CI processes resulting from distinctive mesoscale environments interacting with the complex terrain of central Argentina. We will detail radar and radiosonde data collected during two deployments occurring along the Sierras de Córdoba (SDC) range in the Córdoba province on 29 November and 4 December 2018 (Fig. 1). More detail on instrument deployment, operations, datasets, and quality control can be found in Nesbitt et al. (2021) and Varble et al. (2021).

On 29 November, multiple precipitating convective cells initiate along the east side of the SDC between approximately 1615 and 1715 UTC (1315–1415 local time) (e.g., Fig. 1a). At least five precipitation cores reached a maximum C-band radar reflectivity greater than 50 dBZ at low levels and persisted for a duration between 1 and 2.5 h. A mesoscale radiosonde network consisted of hourly launches between 1300 and 1900 UTC from six mobile facilities (Schumacher 2019; Wurman and Kosiba 2021a) and every three hours from the U.S. Department of Energy Atmospheric Radiation Measurement (ARM) Mobile Facility (AMF) instrument site (Holdridge et al. 2018), collecting full tropospheric thermodynamic and wind profiles prior to and after CI. Two Doppler on Wheels (DOWs; Wurman and Kosiba 2021b) X-band radars and a C-band Scanning ARM Precipitation Radar (CSAPR2; Bharadwaj et al. 2018) collected data east of the SDC near the AMF site. Throughout the deployment, the DOWs collected volumetric plan-position indicator (PPI) scans between 0.5° and 42° antenna elevation angles every 3–5 min. The CSAPR2 scanned PPI volumes between 0.5° and 33°, collecting ~6-min-duration volumes every 15 min. Volume

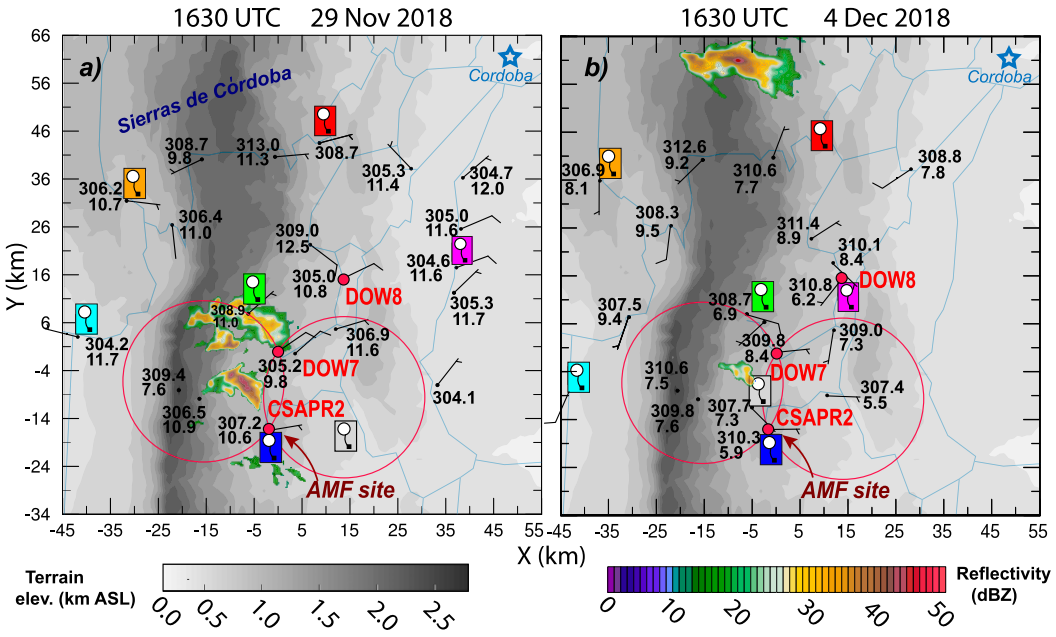

FIG. 1. Instrument deployment maps for the (a) 29 Nov 2018 and (b) 4 Dec 2018 cases. Locations of the DOW 7, DOW 8, CSAPR2 radars, and dual-Doppler lobes are labeled in red. An array of surface observations from radiosondes, ARM surface stations (Kyrouac and Holdridge 2018), Pod surface stations (1-m height) and mobile mesonets (3-m height) (Wurman and Kosiba 2021c,d) are shown in black [θ_v (K) and q_v (g kg^{-1})] and DOW 7 radar reflectivity from the 3.5° beam elevation angle is shaded. Radiosonde launch locations are marked. Location of the ARM AMF site is annotated.

start times for CSAPR2 and the DOWs are synchronized, and the radars are optimally positioned for dual-Doppler wind retrievals surrounding the CI location. Although dual-Doppler retrievals are limited to a 15-min frequency, the 16-km radar baseline yields excellent spatial resolution of the three-dimensional flow.

A similar instrument deployment occurred on 4 December, with only subtle differences in the locations of mobile assets, particularly the radiosondes (Schumacher 2019; Wurman and Kosiba 2021a; Holdridge et al. 2018) (Fig. 1b). The radar network (Bharadwaj et al. 2018; Wurman and Kosiba 2021b) detected surface precipitation associated with a weak convective cell forming at nearly the same local time and geographical location as during the 29 November case. This surface precipitation signal persists for only ~30 min as the cloud moves eastward away from the terrain. Near-surface C-band radar reflectivity does not exceed 35 dBZ for more than 15 min, and thus remains below thresholds utilized by a companion study (Nelson et al. 2021) to classify sustained CI processes. Longer-lived deep convection initiates approximately 60 km north of this cell, outside of the instrument array.

Our third case occurred during the PECAN field experiment, which focused on understanding nocturnal CI over the U.S. central plains (Weckwerth et al. 2019). During the evening of 3 July 2015, an informal CI mission was conducted with a limited instrumentation array deployed near the base of operations for the project at Hays, Kansas (Fig. 2). Three DOWs (Wurman and Kosiba 2018a) were deployed from approximately 0200–0500 UTC (2100–0000 local time), performing synchronized PPI volume scans with the National Center for Atmospheric Research's S-/Ka-band dual-polarimetric radar (SPOLKa; UCAR/NCAR 2016) located near McCracken, Kansas. Radar baselines are approximately 45 km, chosen to cast a large net over an area with large forecast uncertainty. Dual-Doppler volumes are available every 10 min. During this deployment, isolated convective cells develop along a southward-moving east–west-oriented line of enhanced radar reflectivity collocated with a surface wind shift between 0230 and 0430 UTC. Cells initiating at 0230 UTC persist for approximately 45 min, while those initiating at later times persist for 2–3 h. Only two balloon radiosondes were launched during the observing period, at 0300 and 0600 UTC at Ellis, Kansas (Clark 2016). The surface wind shift boundary passes over Ellis at approximately 0200 UTC; therefore, all radiosondes were launched north of it. However, vertically pointing lidar (Clark 2015a), atmospheric emitted radiance interferometer (AERI) instruments (Turner 2016), and surface observations (Clark 2015b) provide high-frequency retrievals of thermodynamic and moisture profiles prior to and after the passage of the wind shift boundary. Finally, two mobile mesonets (e.g., Waugh and Fredrickson 2010; Wurman and Kosiba 2018b) performed transects through the center of the radar domain, collecting 3-m surface meteorological observations across the surface boundary.

Dual-Doppler wind retrievals

Radar radial velocity and reflectivity data from both clear air and precipitating meteorological targets are quality controlled

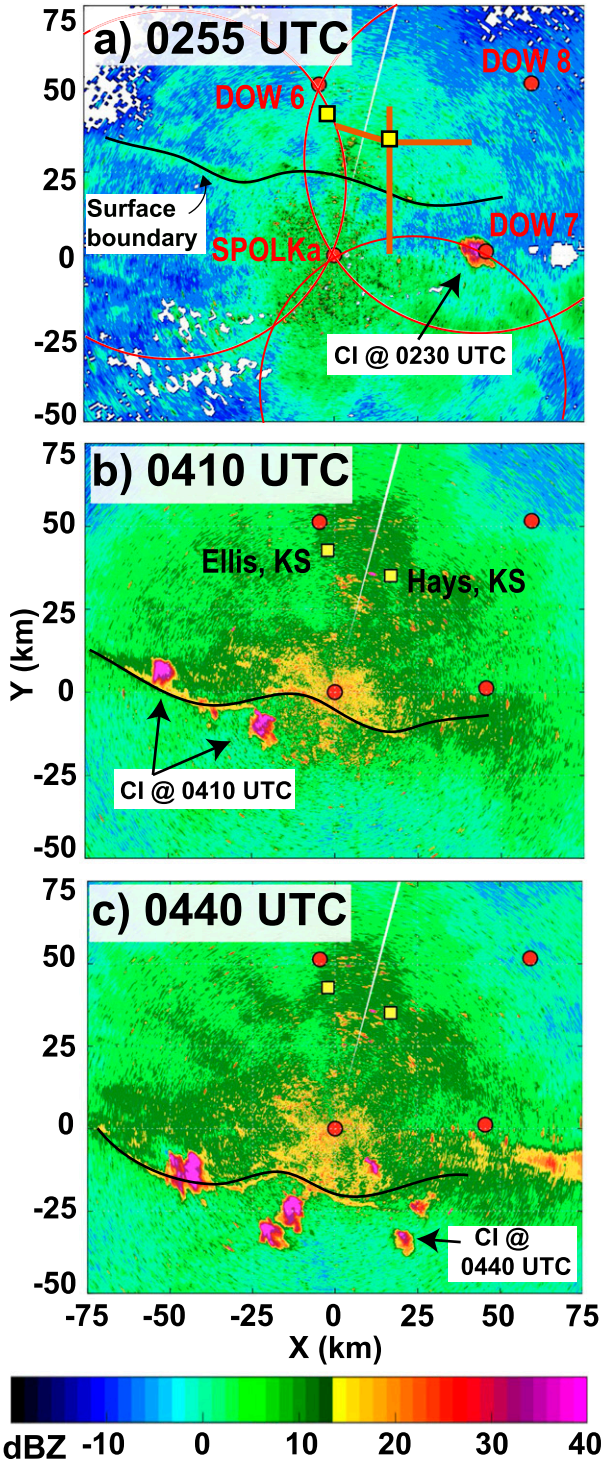

FIG. 2. (a)–(c) Instrument deployment map for 3 Jul 2015. Positions of the SPOLKa, DOWs 6–8 radars, and radiosondes and profilers at Ellis, KS, are shown in each panel. Mobile mesonet transects are shown as brown lines in (a). SPOLKa radar reflectivity is shaded, and the position of the surface boundary is traced at three times between 0255 and 0440 UTC, when CI episodes occur.

to remove ground clutter and side-lobe contamination, signal interference, and other noise. To facilitate dual-Doppler analyses, single-Doppler velocity and reflectivity data are objectively analyzed to a Cartesian grid with a two-pass isotropic Barnes weighting function (Barnes 1964; Majcen et al. 2008). The smoothing is chosen based on the coarsest spatial sampling in the desired domain (Trapp and Doswell 2000). In all cases, the coarsest vertical sampling (2.0°) was larger than the horizontal data sampling (beams widths for the DOWs, SPOLKa, and CSAPR2, are 0.93°, 0.92°, and 1.0°, respectively). The isotropic Barnes smoothing parameter, $\kappa = (1.33\delta)^2$ (Pauley and Wu 1990), where $\delta = R\varphi$, R is the maximum distance between the edge of the desired retrieval domain and each radar, and $\varphi = 2.0°$. The Cartesian grid spacing of the objectively analyzed data, $\Delta \sim \delta/2.5$ (Koch et al. 1983). For the 29 November and 4 December 2018 cases, $\kappa = 0.76\,\text{km}^2$ and $\Delta = 200$ (100) m in the horizontal (vertical). Longer radar baselines during the 3 July 2015 case yield comparatively coarser resolution, $\kappa = 5.94\,\text{km}^2$, $\Delta = 500$ (250) m in the horizontal (vertical). In all cases, a two-pass convergence parameter, $\gamma = 0.3$, is used (Majcen et al. 2008).

We employ a traditional iterative upward integration of the anelastic mass continuity equation in our wind synthesis (e.g., Dowell and Shapiro 2003), applying a lower boundary condition of $w = 0\,\text{m s}^{-1}$. The lowest matched radar horizon in the CI focus regions of the 29 November and 4 December cases is often located within 100 m of the ground because radars scan uphill. The matched horizon is sometimes as high as 1000 m above the ground in the far reaches of the comparatively large 3 July 2015 dual-Doppler lobes. Lacking sufficient coverage from other sources of near-surface winds, we assume that the single-Doppler winds are constant between the lowest matched radar horizon and the ground. A flat terrain lower boundary is prescribed for the 3 July 2015 case, which occurs on the U.S. plains. For the 29 November and 4 December analyses occurring along the SDC, we prescribe the height of the ground using 3-s resolution topography data. Subsequent iterative upward integration of mass continuity is performed starting at the local terrain height at each horizontal grid point.

3. Mesoscale conditions yielding CI

Many studies use radar reflectivity thresholds to quantitatively define the occurrence of CI (e.g., Wilson and Schreiber 1986; Wilson and Roberts 2006; Lima and Wilson 2008; Rasmussen and Houze 2016; Alexander et al. 2018; Nelson et al. 2021). We examine the low-level mesoscale environment and updrafts immediately leading up to and concurrent with the onset of radar-detected precipitation near the ground. A deeper examination of microphysical cloud properties occurring during the CI process is reserved for future research.

a. 29 November 2018—RELAMPAGO-CACTI

Synoptic northeasterly low-level flow from a surface high pressure off the Atlantic coast of Argentina transported moist air toward the Córdoba region. For several hours preceding CI, deep congestus clouds (cloud tops > 4 km above sea level; hereafter ASL) develop just east of the SDC ridgeline, with shallow cumulus (cloud tops < 2 km ASL) west of the ridgeline

and comparatively few clouds directly over it (e.g., Fig. 3a). Dual-Doppler wind retrievals indicate mean low-level upslope flow and $O(1)$-km-wide convergence and divergence perturbations suggesting shallow dry CBL cellular or roll circulations that dominate the overall signal of horizontal convergence (Figs. 4a–c). There is not an obvious continuous swath of near-surface convergence aligned with the terrain, nor one associated with a surface air mass boundary. Rather, a pattern of convergence and divergence resembling the CBL circulations occurring over the lower terrain is also found near the higher terrain. This is consistent with past studies that find ascent from $O(1)$-km-wide CBL circulations can dominate the signal of the comparatively meager background mesoscale ascent associated with the terrain-induced flow (e.g., Raymond and Wilkening 1980; Demko and Geerts 2010). The low-level northeasterly flow in the dual-Doppler domain increases by 4–5 m s^{-1} in the 30–45 min preceding the first radar-detected surface precipitation echoes, and there is perhaps a subtle reduction in the amount of near-surface divergence along the leading edge of the upslope winds where it meets comparatively stagnant winds to the west (along $x \sim -15$ km in Figs. 4a,b). This leading edge of the northeasterly winds is coincident with the location of deepening cumulus prior to 1630 UTC (purple contours in Figs. 4a,b).

To highlight mesoscale structure of thermally induced orographic flow whose signal is obscured by CBL eddies, we examine along-peak averages (over the range $-25 < y < 5$ km in Fig. 4) of the flow (similar to Demko and Geerts 2010). The meridional mean of the flow perpendicular to the SDC on 29 November illustrates that the northeasterly upslope winds are confined to a shallow layer ($z < 0.75$ km above ground level; hereafter AGL) on the eastern slope of the SDC (Figs. 5a,b). Prior to CI, shallow meridional-mean low-level convergence (~750 m deep) is occasionally detected near the ridgeline, located within weak winds in the lowest 3–3.5 km ASL (below 1–1.5 km AGL near the ridge top) rather than at the leading edge of the shallow upslope flow (Figs. 5a–c). This early shallow convergence signal may result from thermally induced orographic flow in response to solar heating of the terrain (e.g., Kirshbaum 2013). If significant convergence is associated with the upslope flow, it may be too shallow and close to the ground to detect at this time. However, meridional-mean convergence deepens to ~1.25–1.5 km AGL after 1630 UTC, as the previously shallow upslope flow strengthens and deepens (by ~2.5 m s^{-1} and ~600 m, respectively), and reaches the ridgeline (Figs. 5d,e). The first near-surface precipitation radar echoes greater than 35 dBZ occur approximately 10 km east of the ridgeline between 1615 and 1630 UTC, as the shallow layer of upsloping winds begins to deepen and strengthen there. Though meridional mean low-level convergence and updraft is found along many potions of the eastern slopes throughout the observing period, new deep cumulus and CI episodes occur closer to the ridgeline after 1630 UTC (Fig. 3c) as the leading edge of the upslope flow approaches it. Flow from one such precipitating updraft is present within the meridionally averaged flow at 1700 UTC as it travels eastward (e.g., centered at $x \sim -10$ km in Fig. 5e), and should not be confused for a longer-wavelength terrain-induced mesoscale circulation.

Observations and supportive simulations of terrain-induced flow by Banta (1984, 1986) reveal leeside convergence supportive of cloud formation. In those studies, a morning erosion of the nocturnal boundary layer results in a downward mixing of westerly momentum that pushes the leeside upslope flow and convergence at its leading edge downstream of the terrain crest. Seemingly, the opposite trend is observed during 29 November, where upslope flow progresses uphill into a layer of relatively weak flow present up to ~1 km above the ridgeline. We speculate in this case that the uphill progression of upslope flow may result from a combination of factors related to a thermally forced solenoidal orographic circulation and strengthening of the background meso- to synoptic-scale northeasterly flow in the afternoon (i.e., a ''mechanical'' forcing) (Kirshbaum et al. 2018), the latter of which does not appear to be directly represented by the simulations of Banta (1986). However, larger-scale low-level flow factors aside, it is possible that the continued upward progression of upslope flow on 29 November is consistent with Banta (1986) simulations because of the relatively stagnant horizontal winds located in a 0–1.5-km-deep layer above the ridgeline between 1500 and 1700 UTC. In this situation, daytime convective mixing does not encounter significant westerly momentum to transport downward to oppose the upslope flow.

It is difficult to definitively evaluate the degree of thermally forced flow symmetric about the terrain because of the relative paucity of data west of the ridgeline. Radiosonde observations directly west of the dual-Doppler region (cyan profile in Figs. 5a,e) indicate low-level westerlies of similar magnitude to the easterly upslope flow. This limited wind data may suggest shallow anabatic flow that is partly symmetric about the ridgeline, consistent with the existence of an orographic solenoidal circulation. If both thermally and mechanically forced flows are generating convergence near the ridgeline, they may combine to support the evolution of cloud development and CI. This bears similarity to conclusions made by studies of the 15 July 2007 CI event occurring in the Black Forest Mountains during COPS (Kalthoff et al. 2009; Behrendt et al. 2011; Khodayar et al. 2013).

Examination of synchronized radiosonde launches illustrates spatial heterogeneity of static instability and moisture surrounding the forecasted CI location (Fig. 6). The boundary layer[1] is topped by an elevated statically neutral layer (between ~830 and 700 hPa, depending on the radiosonde launch site), with considerable moisture heterogeneity present across the sounding array (e.g., water vapor mixing ratio q_v spans 1.8–6.8 g kg^{-1} at 775 hPa). Significant low-level mean layer (ML[2]) CIN is

[1] We quantify boundary layer depth using the method described by Liu and Liang (2010), which detects the first height at which the vertical gradient of potential temperature exceeds 4 K km^{-1}.

[2] Sounding parameters are calculated by lifting a parcel assumed to have mean thermodynamic properties found in the lowest 100 hPa of the atmosphere. ML metrics are used over those calculated from parcels originating at a single height to partly account for mixing of boundary layer air into low-level updrafts (e.g., Craven et al. 2002; Markowski and Richardson 2010).

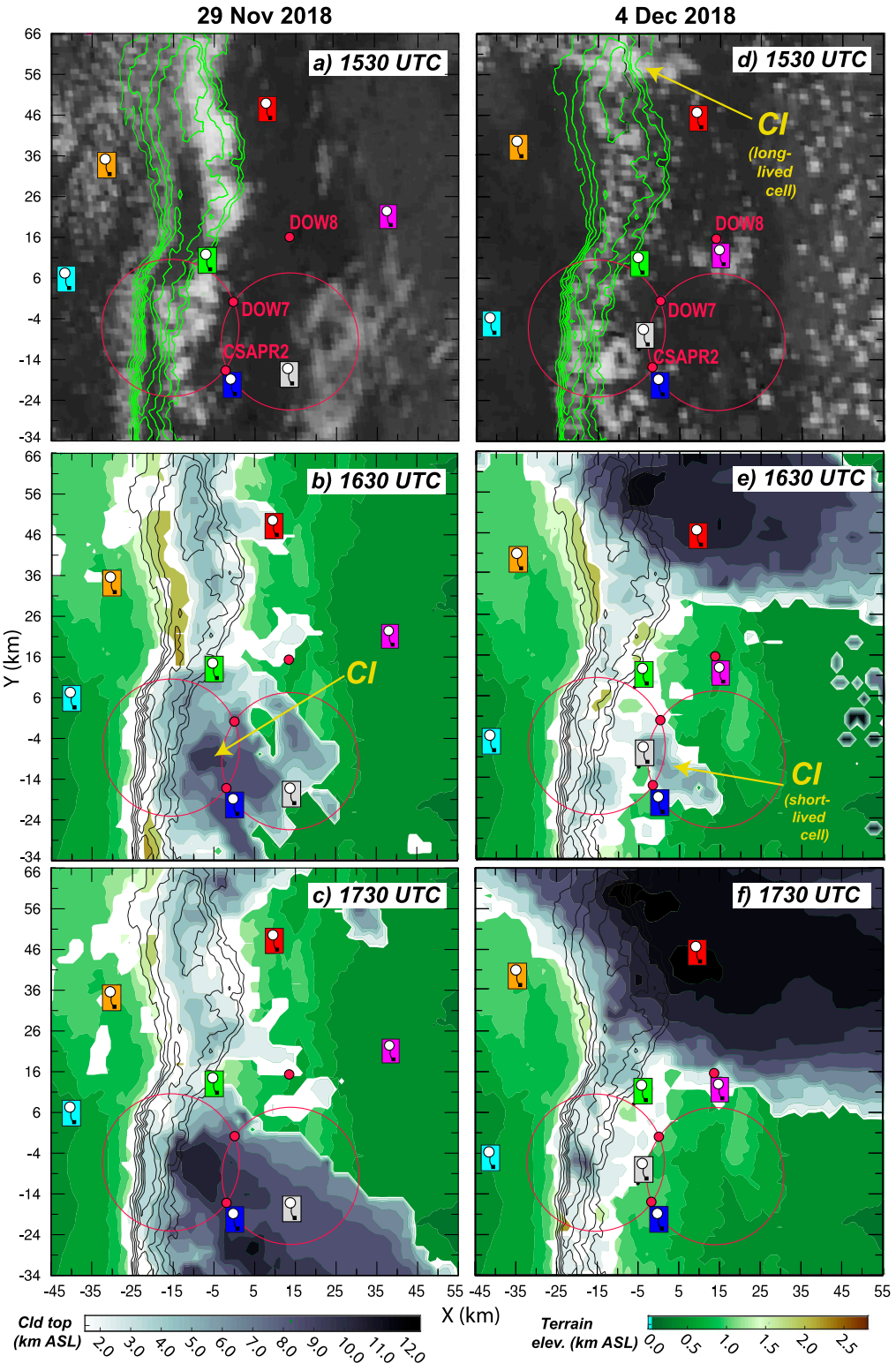

FIG. 3. (a),(d) *GOES-16* visible radiance at 1530 UTC (UCAR/NCAR 2019) and (b),(c),(e),(f) cloud top height derived from GOES infrared brightness temperature at 1630–1730 UTC (ARM 2018) on (left) 29 Nov and (right) 4 Dec 2018. Surface elevation above sea level is shown in green–brown shading in (b), (c), (e) and (f) and with contours (outermost contour is 1.5 km above sea level, incremented by 0.2 km) in green in (a) and (d), and in black in (b), (c), (e), and (f). Radiosonde launch sites and radar positions are shown in all panels. Locations of CI events discussed in the text are annotated in (b), (d), and (e).

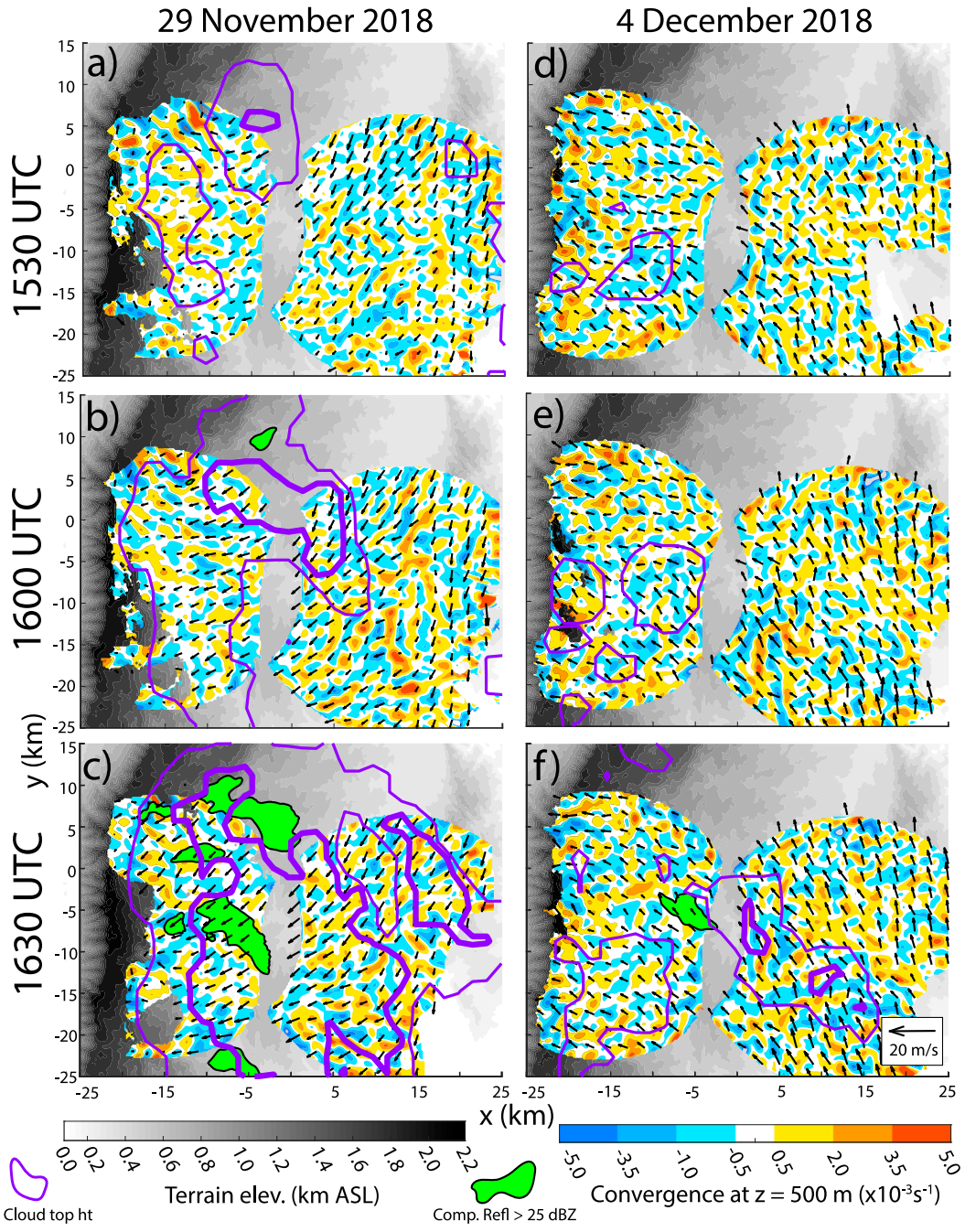

FIG. 4. Dual-Doppler horizontal flow convergence at 500 m AGL (shaded), column maximum DOW X-band radar reflectivity > 25 dB*Z* at 500 m AGL (magenta), and GOES-estimated cloud top height (purple contours) at 3 (thin) and 6 (thick) km ASL. Plots are valid between 1530 and 1630 UTC (left) 29 Nov and (right) 4 Dec. Surface elevation above sea level is shaded in gray.

present over the lowest terrain, where the boundary layer and overlying elevated neutral layer are the most decoupled. CI occurs within 10–15-km horizontal distance of the highest portion of the ridgeline (located at $y = -6$ km in Figs. 1, 3, and 4), near where relative humidity is highest, and ML LFC and CIN are minimized (green and blue profiles in Fig. 6a).

Relative humidity steadily increases in the upper boundary layer and lower free troposphere leading up to CI as a result of increasing specific humidity (Fig. 6b). This moistening corresponds to deepening upslope flow and possibly with moist updrafts and clouds detraining into the lower free troposphere (the soundings shown in Fig. 6b are launched near the cloud line that is continuous with the convergence line retrieved

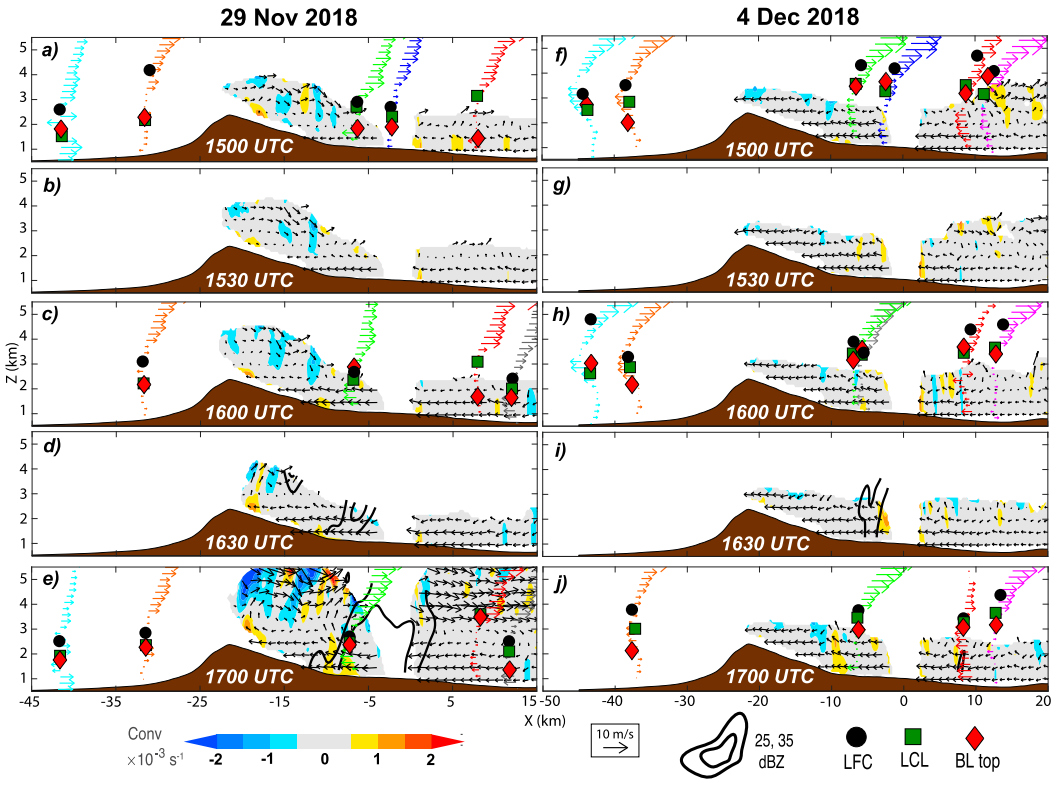

FIG. 5. Cross sections of dual-Doppler meridional-mean zonal and vertical wind (vectors), horizontal convergence (shaded), and DOW radar reflectivity (25 and 35 dBZ; thick black contours) between 1500 and 1700 UTC (a)–(e) 29 Nov 2018 and (f)–(j) 4 Dec 2018. Radiosonde-measured horizontal winds (vector profiles colored to match launch sites shown in Fig. 1), boundary layer depth (red diamonds; measured as in Liu and Liang 2010; Nelson et al. 2021), ML LCL (green boxes) and ML LFC (black circles) measured from hourly radiosondes are projected into the cross section. The meridional-mean terrain profile of the SDC is shown in brown.

within the dual-Doppler lobes; Figs. 3a–c). A shallow elevated temperature inversion located at 600 hPa erodes between 1300 and 1500 UTC, reducing the ML LFC (from 3165 to 1592 km AGL) in the 1–3 h preceding CI. At most times leading up to CI, the ML CAPE was steadily increasing by ~150 J kg^{-1} h^{-1} and ML CIN was <20 J kg^{-1}. Initiation of the most sustained convection occurs between 1630 and 1715 UTC when the meridional-mean convergence along the terrain is most consistently deep and reaches heights that are most similar to the nearest radiosonde-measured environmental ML LFC height (Figs. 5a–e). This observation leads us to hypothesize that an environment where the LFC is similar to the depth of mesoscale ascent supports CI, possibly because it minimizes the depth over which parcels must rise before the production of buoyancy within an updraft, offsetting loss by free tropospheric entrainment (e.g., Houston and Niyogi 2007).

b. 4 December 2018—RELAMPAGO-CACTI

On 4 December, a surface low pressure off of the Atlantic coast and a high pressure in southern Argentina yielded southeasterly low-level flow in the Córdoba province along and east of the SDC. This case shares some common elements with the 29 November case; e.g., O(1)-km CBL cell or roll circulations are evident throughout the dual-Doppler coverage, and there is no visibly obvious band of mesoscale convergence (Figs. 4d–f). Subtle meridional-mean boundary layer convergence (~0.001 s^{-1}) is located within the upslope flow near the longitude of weak CI (near $x = -8$ km in Figs. 5f–j). However, unlike the 29 November case, the upslope component of the background flow is steady (at ~3 m s^{-1}) and deep (below 1.5 km AGL) throughout the deployment rather than increasing and deepening leading up to CI. Easterly winds are observed by radiosondes launched 20–30 km west of the ridgeline, suggesting steady cross-terrain flow (orange and cyan profiles in Figs. 5f–j). Meridional-mean low-level convergence is only ~750 m deep near the highest terrain. It is possible that mesoscale updraft is located above the shallow clear air returns near the ridgeline, or it is displaced westward or partly disrupted by cross-peak flow, similar to the "ventilation regime" simulated by Kirshbaum (2013). Regardless, the majority of cumulus on this day form and deepen directly over the ridgeline (Figs. 3d–f), and the weak and short-lived surface precipitation echo (<35 dBZ lasting <30 min) occurs as it travels away from the terrain after 1615 UTC in the westerly flow aloft (e.g., Figs. 3e, 4e,f).

Vapor mixing ratio varies by ~3 g kg^{-1}/30 km across the radiosonde launch sites in the well-mixed boundary layer (below ~800 hPa; Fig. 7a). Radiosondes launched farthest west

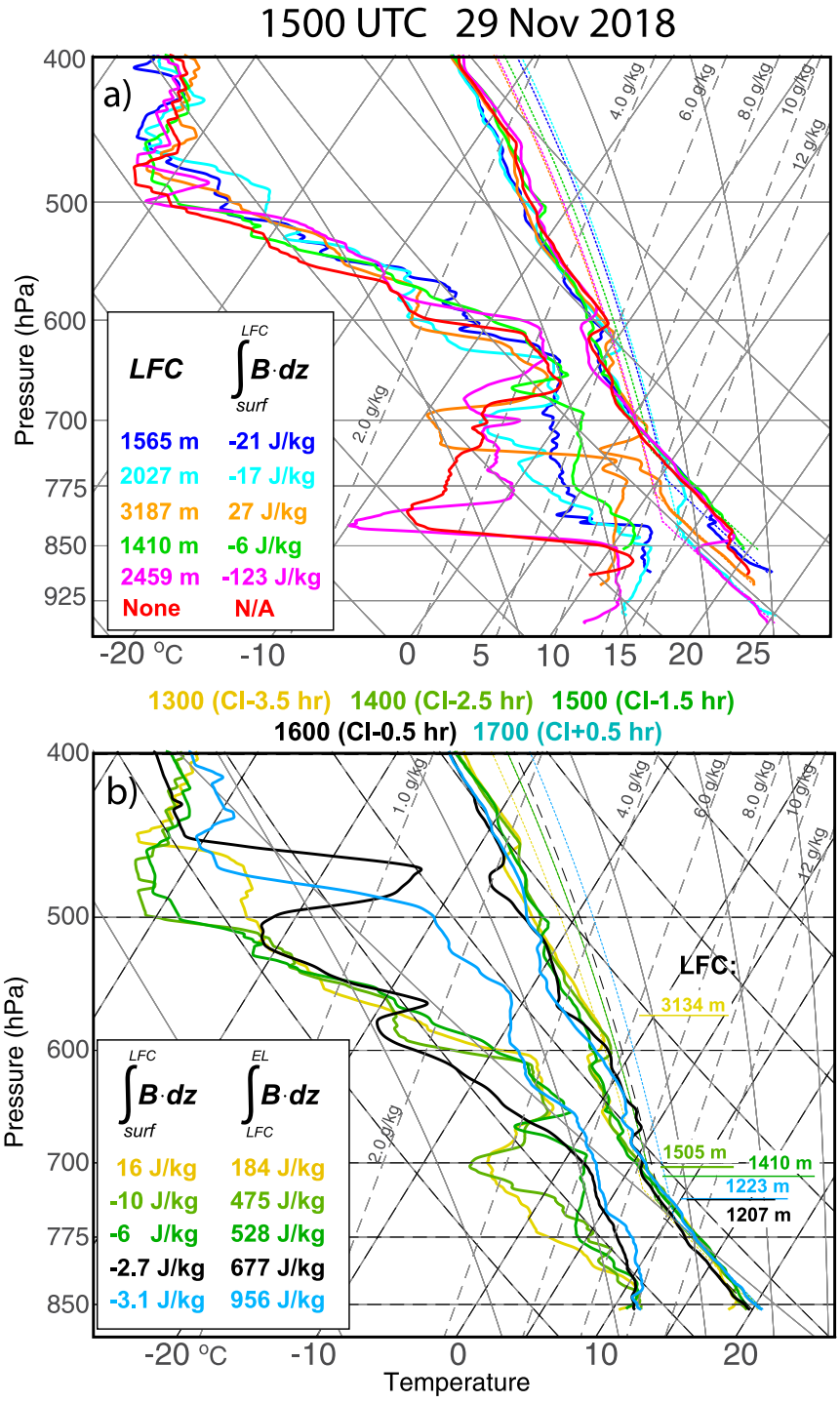

FIG. 6. (a) Skew *T*–log*p* diagrams from six synchronized radiosonde launches at 1500 UTC 29 Nov 2018. Sounding profiles are colorized to match launch sites mapped in Fig. 1a. ML CIN and LFC (AGL) are shown in the bottom-left legend. (b) As in (a), but for sequential hourly radiosonde launches nearest to the CI location (green radiosonde launch site in Figs. 1a and 3a–c) between 1300 and 1700 UTC. Time evolution of the ML CIN and CAPE are shown in the legend, and ML LFC is labeled at each time on the right side of the image.

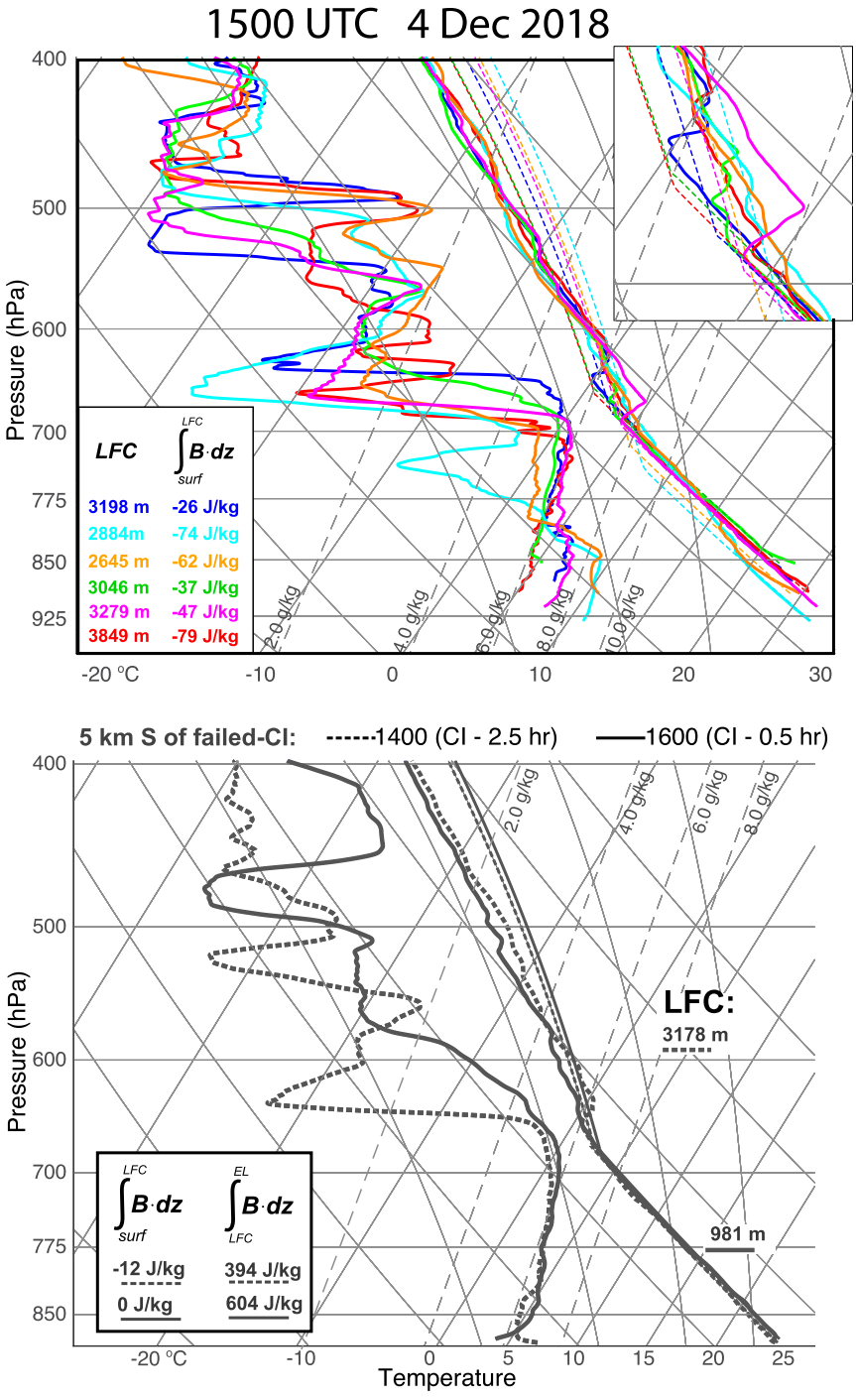

FIG. 7. (a) As in Fig. 6, but for the 4 Dec 2018 case. Soundings are colored to match launch sites shown in Fig. 1b. The area of the soundings between the LCL and LFC is enlarged in an offset in the top right of the panel. (b) Radiosonde launches at 1400 (dashed) and 1600 UTC (solid) from the location closest to the short-lived convective cell (gray launch location in Fig. 1b).

and east of the SDC ridgeline measure well-mixed near-surface profiles decoupled from elevated mixed layers located between 800 and 700 hPa (e.g., orange and cyan profiles in Figs. 5f, 7a), whereas soundings launched nearest to the SDC ridgeline suggest a coupling of these mixed layers (red and green profiles in Figs. 5f, 7a). Thus, in both RELAMPAGO-CACTI cases, surface-based boundary layers and elevated neutral layers are more readily coupled over higher terrain than at lower elevation. However, this condition does not appear to be sufficient for sustained CI. There is considerable variability in the

vertical structure of static stability within the 700–600-hPa layer, resulting in up to 1-km differences in the ML LFC and ~50 J kg^{-1} differences in ML CIN across the sounding sites prior to CI (Fig. 7a). CI occurs nearest to the sounding launch locations measuring the smallest ML CIN preceding it. Consecutive soundings collected within 5 km of the weak and short-lived convective cell reveal steady well-mixed profiles of virtual potential temperature θ_v and q_v (Fig. 7b). Preceding this convective cell, the capping inversion erodes, eliminating ML CIN, and the free troposphere moistens (between 700 and 500 hPa). Despite these favorable conditions, CI processes do not yield sustained convection.

Overall, boundary layer tops and ML LFC east of the terrain are ~1 km higher on this day than on 29 November. The peak surface sensible heat flux measured at the AMF site is ~50 W m^{-2} (~20%) smaller on 4 December than on 29 November (not shown; McCoy et al. 2018). The depth of the surface-based well-mixed moisture layer from the 1500 UTC AMF radiosonde is similar across these days (between the surface and ~800 hPa; cf. blue profiles in Figs. 6a, 7a), but becomes as deep as the statically neutral profile by the next AMF radiosonde launch (1800 UTC; not shown). Thus, the boundary layer depth estimated by the Liu and Liang (2010) method jumps as the coupled surface-based and elevated neutral layers become indistinct. Conflating these two statically neutral layers is perhaps academic from the static stability perspective of a dry CBL updraft that is ascending through a uniform neutral low-level profile, but there may be ramifications for evaluating entrainment-driven dilution of the low-level updraft as it ascends through a vertically inhomogeneous q_v profile in the lower troposphere prior to it mixing over the full depth of the coupled neutral layers.

c. 3 July 2015—PECAN

Unlike the 29 November and 4 December 2018 events with CI occurring in orographic flow, CI on 3 July 2015 is observed along a surface wind shift boundary over flat terrain with organized horizontal flow convergence (Fig. 8). This boundary is observed within weak synoptic northeasterly surface winds far north of a surface stationary front located in central Oklahoma. AERI, lidar, and radiosonde measurements collected at Ellis, Kansas, illustrate the vertical structure of the wind shift boundary as it passes by the site at 0200 UTC (Fig. 9). Leading the boundary (south of it), isolated boundary layer updrafts of up to 1.5 m s^{-1} are measured between the surface and ~1.75 km AGL (the typical ceiling of reliable data). A similar updraft depth is suggested by contemporaneous lidar measurements made at Hays, Kansas (not shown; Wagner et al. 2016a,b). Assuming steady flow structure in time, the wind shift boundary is approximately 1 km deep 1 h after its passage, and approximately 1.5 km deep 3–4 h after passage (Fig. 9a). Horizontal flow convergence along the boundary extends up to ~1 km AGL. Steady surface cooling occurs at Ellis, Kansas, starting about an hour ahead of the wind shift and continues well after its passage (Fig. 9b). This cooling is likely a result of nocturnal radiative cooling (a shallow near-surface inversion develops between 0300 and 0600 UTC; green and red profiles in Fig. 10) rather than a significantly cooler northern air mass.

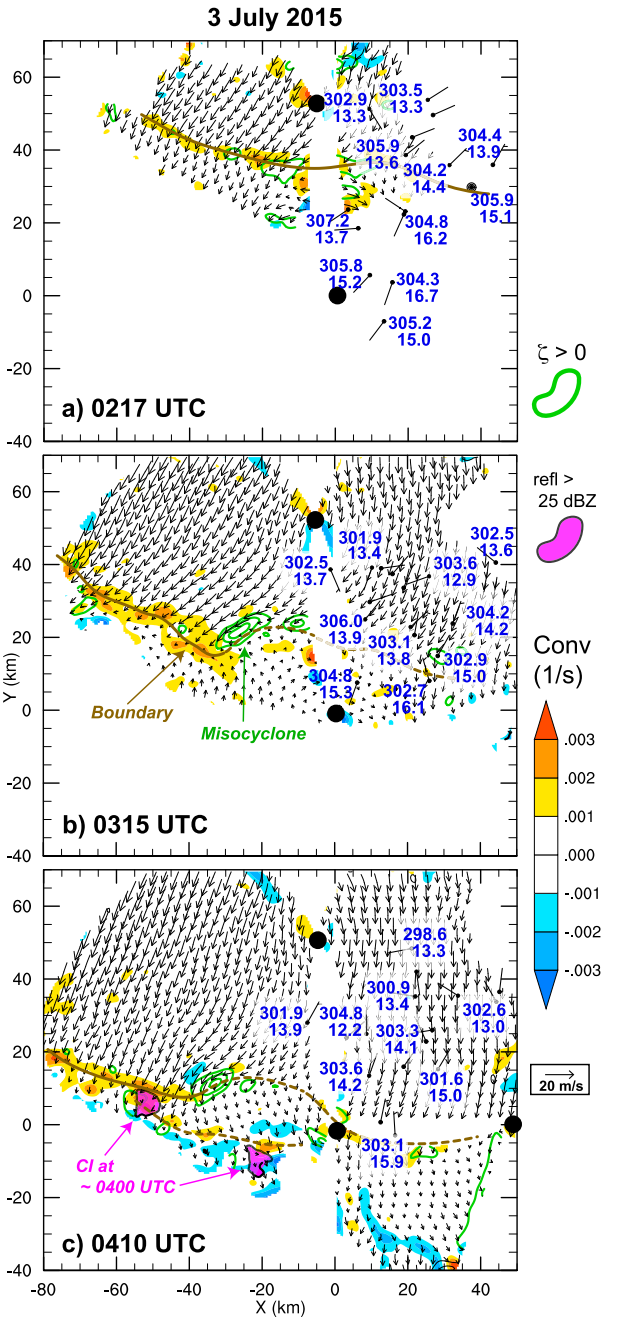

FIG. 8. Horizontal flow convergence (shaded), ground-relative horizontal winds (vectors), and positive vertical vorticity (green contours; every 0.001 s^{-1}) calculated from quasi-2D dual-Doppler retrievals (using only the lowest level radar scans) between 0217 and 0410 UTC 3 Jul 2015. These quasi-2D analyses isolate the structure of the boundary at the lowest radar-observed levels. 3-m θ_v (K), q_v (g kg^{-1}), and horizontal wind (m s^{-1}; barbs) observations from mobile mesonets with positions adjusted with a time-to-space conversion within 60-min windows using the estimated mean boundary motion of $(u, v) = (-3.5\ \text{m s}^{-1}, -3.5\ \text{m s}^{-1})$. Positions of the radars shown in Fig. 2 are highlighted with black dots. SPOLKa radar reflectivity > 25 dBZ is shown in magenta.

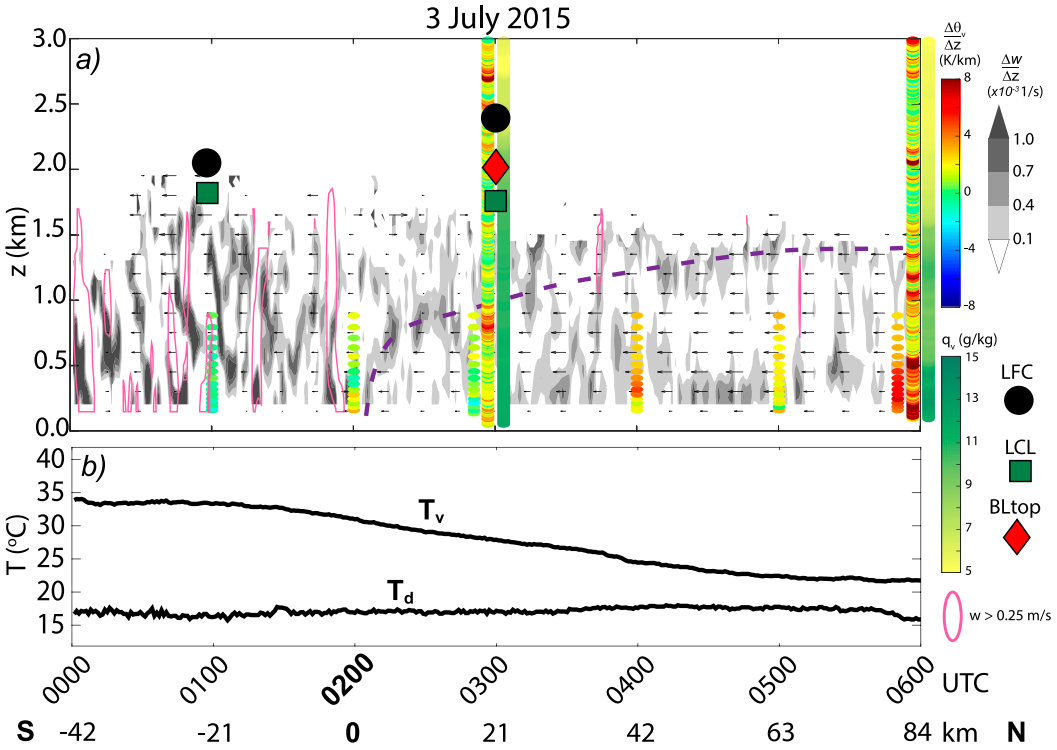

FIG. 9. (a) Lidar-retrieved boundary-relative meridional wind profiles (vectors), the vertical gradient of lidar-measured vertical velocity approximating horizontal wind convergence (shaded), lidar-measured updraft (>0.25 m s^{-1}; magenta contour), AERI static stability profiles below z = 850 m (shown hourly), and radiosonde static stability and q_v profiles from the 0300 and 0600 UTC radiosondes located at Ellis, KS. Radiosonde-estimated (and combined radiosonde-AERI-estimated at 0100 UTC) ML LCL (green boxes), ML LFCs (black circles), and the 0300 UTC boundary layer top [red diamond; calculated with the Liu and Liang (2010) method] are overlaid. (b) Surface virtual temperature and dewpoint temperature observations. Boundary-relative winds are calculated and meridional distance (horizontal axis) is time–space converted using the mean meridional motion of the boundary, $v = -3.5$ m s^{-1}. Depth and slope of the wind shift boundary (purple dashed line) is subjectively estimated using wind, convergence, and radiosonde stability profiles.

Time-to-space-converted mobile mesonet tracks show subtle θ_v gradients across the surface wind shift, ~ −2 K/40 km (Fig. 8). However, it is difficult to determine an accurate instantaneous temperature differential across the wind shift because of the 60-min time-to-space conversion window.

To assess changes in static stability and moisture across the boundary, we use both radiosonde and AERI soundings. The AERI profiles most closely match contemporaneous balloon radiosonde profiles between the surface and approximately 850 hPa (Fig. 10); thus, we focus our attention on AERI data collected in this layer. AERI profiles collected ahead of and shortly after the passage of the surface wind shift indicate nearly statically neutral conditions (Figs. 9a, 10), suggestive of a well-mixed boundary layer preceding the wind shift. The 0300 UTC radiosonde measures a layer of nearly statically neutral lapse rates and high q_v (~13 g kg^{-1}) between the top of the wind shift boundary and z = 2 km AGL that extends almost all the way to the ML LFC (z = 2.2 km AGL). This deep moisture layer may be partly a result of lofted low-level moisture located ahead of the wind shift, analogous to isentropic frontal overrunning (e.g., Weckwerth et al. 2019; Miller et al. 2020); however, deep moisture measurements are not available ahead of the surface boundary to confirm this vertical transport. Regardless, this elevated moisture above the wind shift boundary may have helped CI by mitigating dilution of buoyancy within low-level updrafts occurring along the boundary.

With a significant 100-hPa-deep midlevel temperature inversion and cool air behind the boundary, there is 351 (54) J kg^{-1} of ML CAPE (CIN) measured by the 0300 UTC Ellis radiosonde (Fig. 10). A sounding approximating the environment just ahead (south) of the boundary, synthesized by combining the 0100 UTC AERI profile below 850 hPa and the Ellis 0300 UTC radiosonde profile above 775 hPa (assuming well-mixed θ_v and q_v profiles between 850 and 775 hPa; solid blue profile in Fig. 10) contains nearly 680 J kg^{-1} of ML CAPE and only 5.0 J kg^{-1} of ML CIN. Thus, parcel theory suggests that air ahead of the surface boundary contains sufficient convective potential to surpass the formidable midlevel inversion; whereas, parcels originating from behind the boundary may not. The deepest radar echoes (>35 dBZ) measured by the SPOLKa range–height indicator scans reach z ~8 km

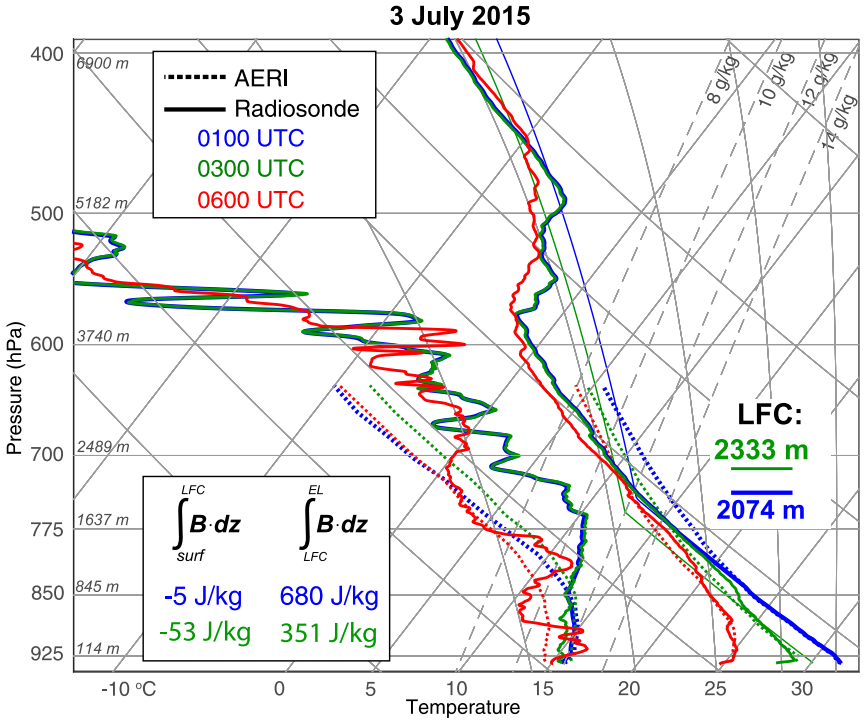

FIG. 10. Skew T–log$p$ diagrams from radiosonde and AERI measurements between 0100 and 0600 UTC 3 Jul 2015. Radiosonde profiles are shown with solid lines and AERI profiles are shown with dashed lines. The solid blue profile is a combination of low-level AERI data valid at 0100 UTC and the 0300 UTC radiosonde aloft (described in the text). ML CIN and CAPE from 0100 to 0300 UTC are shown in the bottom-left offset. ML LFC (AGL) is labeled on the right. For reference, the altitude AGL (mean of each sounding) is shown along each potted pressure level.

AGL, about 4.5 km below the equilibrium levels estimated by the 0100 and 0300 UTC soundings (not shown). Processes unaccounted for by parcel theory assumptions may affect this disparity in expected cloud depth, including entrainment of relatively dry air from the free troposphere within the midlevel inversion layer where updraft buoyancy is locally minimized.

There are several areas of vertical vorticity located along the surface wind shift, moving slowly westward along it as the boundary moves southward (Fig. 8). These patches of enhanced vertical vorticity qualitatively resemble ''misocyclones'' described by past studies (e.g., Weckwerth and Wakimoto 1992; Lee and Wilhelmson 1997; Marquis et al. 2007; Buban et al. 2012) that have sometimes been hypothesized to serve as focal points for enhanced updraft, cloud development, and CI (e.g., Lee et al. 2000; Arnott et al. 2006). However, the prominent circulations in the 3 July case are larger (~6 × 10 km in areal extent) and generally weaker (peak vorticity ~0.001–0.003 s^{-1}) than in past studies. Between 0230 and 0400 UTC, two neighboring circulations merge into a larger oblong one whose major axis is oriented ~45° offset from the east–west-oriented surface boundary. This resulting circulation locally contorts and enhances convergence along the surface boundary (Fig. 8b), as in Marquis et al. (2007). Ultimately the circulation becomes detached from the original convergence boundary, lingering to the north and becoming part of a complex apparent double convergence line structure (brown dashed lines in Fig. 8c). One episode of CI on this day occurs approximately 15 km west of the large circulation, near the intersection of the two apparent lines, where low-level convergence is stronger and wider than elsewhere (Fig. 8c). Thus, we hypothesize that this complex circulation locally augments the structure of the boundary to promote CI.

4. Updraft properties

In addition to mapping mesobeta-scale flow comprising the near-cloud environment, the dual-Doppler observations provide measurements of updraft size and strength during CI. During the 29 November case, the first dual-Doppler-detected low-level updrafts associated with the CI process are located approximately 5–7 km east of the SDC ridgeline at 1615 UTC (Fig. 11a). There are two 2–3-km-wide updraft patches (area estimated using the $w > 1\,m\,s^{-1}$ contour) located along the low-level maximum horizontal velocity gradient tensor approximating the location of the leading edge of the enhanced upslope flow (e.g., Stonitsch and Markowski 2007). The peak magnitude of these updrafts (cells ''A'' and ''B'' in Fig. 11) is between 3 and 5 $m\,s^{-1}$ at z = 1.5 km AGL. During their initial precipitation

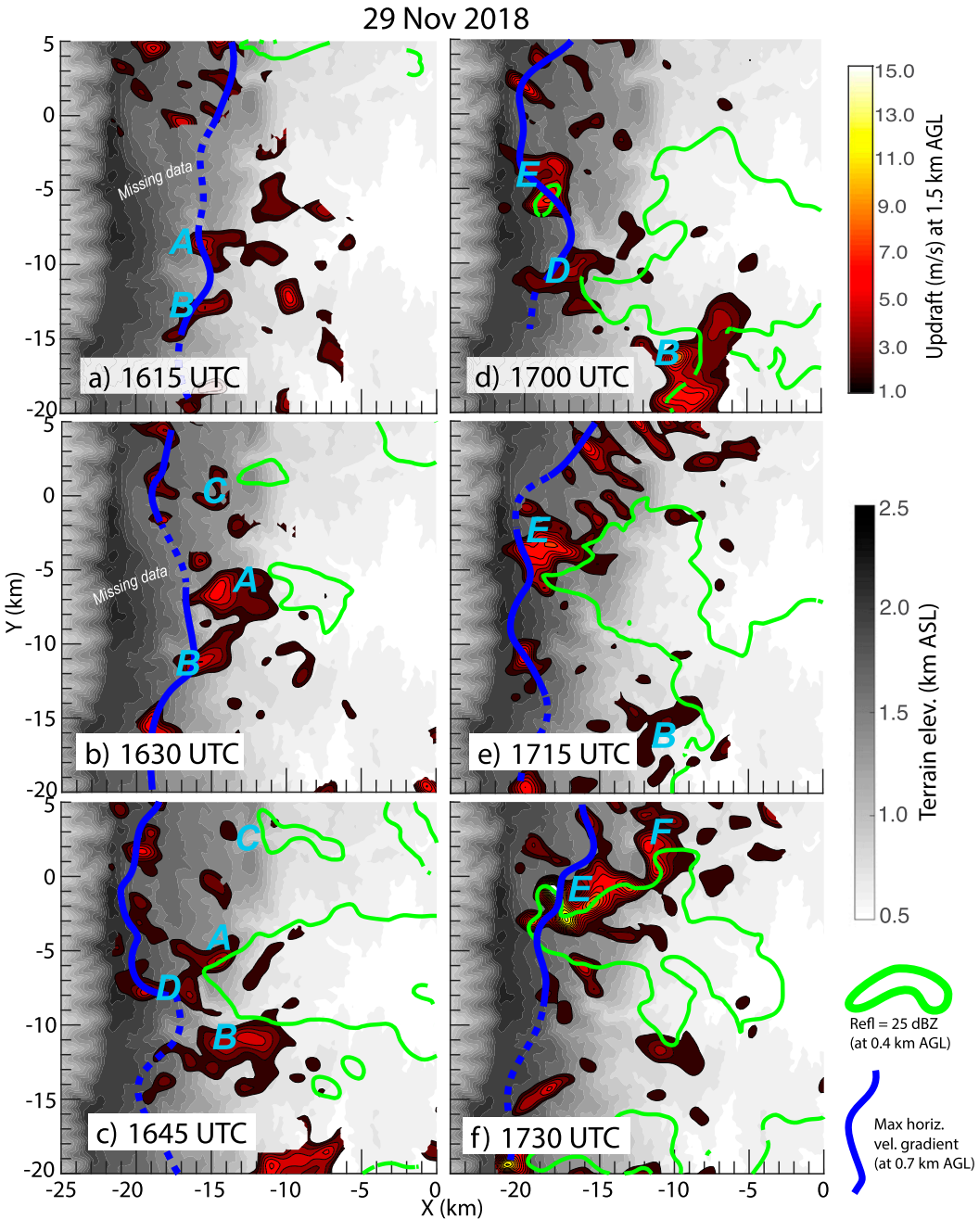

FIG. 11. Dual-Doppler-retrieved vertical velocity at z = 1.5 km AGL (red–yellow shaded) and DOW radar reflectivity at z = 400 m AGL (25 dBZ; green contour) between 1615 and 1730 UTC 29 Nov 2018. Terrain elevation is gray shaded. Subjectively tracked precipitating updrafts described in section 4 are labeled "A"–"F." Subjective trace of the maximum horizontal velocity gradient tensor at z = 700 m AGL, approximating the leading edge of enhanced upslope flow, is shown with a blue line (dashed where there is missing data or uncertainty).

formation between 1615 and 1645 UTC, these updrafts grow to a width of ~5 km (Figs. 11a–c). Multiple updrafts and precipitation cores develop along or very near to the surface upslope wind shift near the ridgeline during the next 1.5 h, and many shallow boundary layer updrafts east of the CI locations are suppressed within the area containing precipitation (Figs. 11c–f). Some cells follow a similar evolution to cells A and B, where areas of 1–3-km-wide updrafts develop into more coherent larger 3–5-km-wide ones (e.g., cell "E" in Figs. 11c–f). Other smaller and shorter-lived cells are associated with 1–3-km-wide updrafts that dissipate shortly after formation (e.g., cell "C" in Fig. 11).

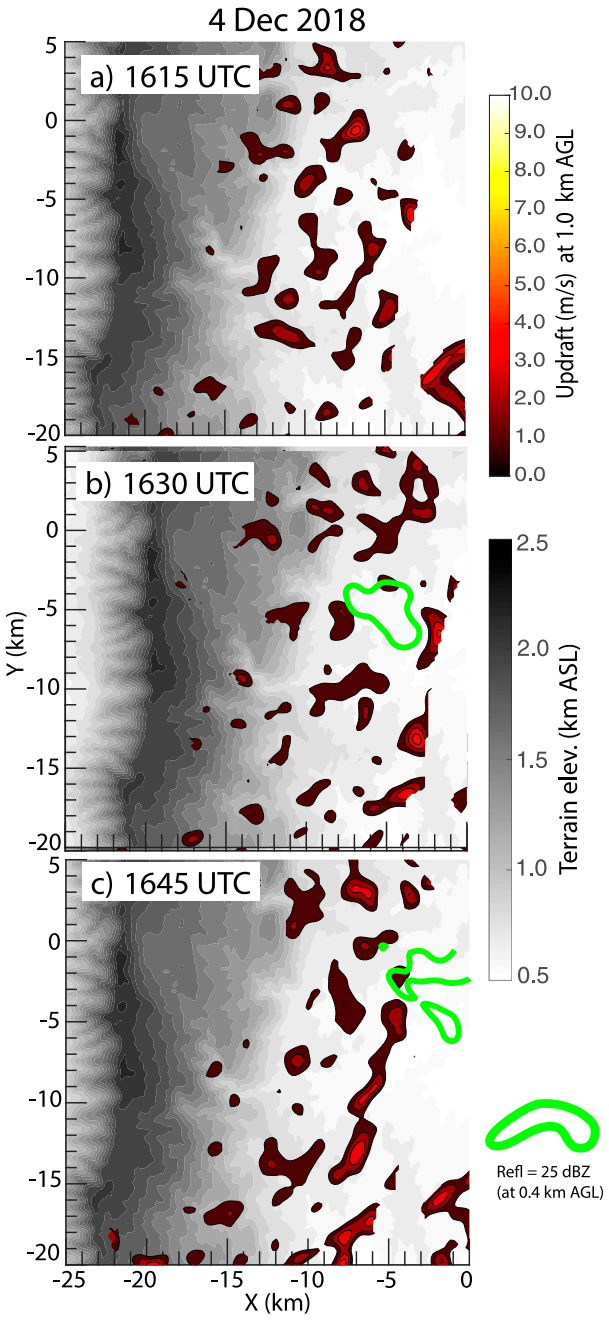

FIG. 12. As in Fig. 11, but valid between 1615 and 1645 UTC 4 Dec 2018. Updrafts are shown at $z = 1.0$ km AGL because of the vertical coverage of available dual-Doppler data.

It is difficult to decisively identify a singular low-level updraft that is associated with the cloud responsible for producing the short-lived precipitation on 4 December (Fig. 12). Instead, only 1–3-km-wide low-level updrafts associated with CBL thermals are evident surrounding the precipitation. We hypothesize that a primary factor yielding unsustained CI in this case is the lack of a sustained low-level updraft larger than those associated with surrounding CBL thermals. From dual-Doppler measurements, CBL thermals in the 4 December case are similar in horizontal size, magnitude, and distribution to the 29 November case (cf. Figs. 4a–f); thus, processes precluding a wide updraft and successful CI do not appear to result from a lack of vigorous CBL activity.

The dual-Doppler-estimated updraft on 3 July 2015 has a diameter of approximately 5 km at $z = 1.25$ km AGL 20 min prior to the first radar-detected precipitation (Fig. 13d). During the next 20 min, multiple similarly sized updrafts develop nearby within a $\sim 10 \times 10\,\text{km}^2$ area along the boundary (Figs. 13e,f). However, the exact updraft sizes are expectedly somewhat uncertain because they are subject to the relatively coarse spatial resolution of the dual-Doppler analyses and their location near the southern fringe of adequate clear air radar signal results in a fairly high matched radar horizon (750–1000 m AGL). It is similarly difficult to objectively quantify the width of the mesoscale boundary at the time of CI for these reasons, but also because the lowest radar beam may be overshooting the top of the surface boundary signal and because of the presence of contortions by circulations and other small-scale variations along it. We estimate the width of the low-level wind shift boundary 1–1.5 h prior to CI, when it is more ideally located within the dual-Doppler coverage, to be 4–6 km (Figs. 13a,b). Subsequent widening of the convergence swath to between 6 and 8 km occurs west of the most prominent circulation during the 0300–0330 UTC period (Figs. 8b, 13c). We hypothesize that this increased width of the convergence along the boundary may have promoted locally wider individual or clustered updrafts that resulted in convective precipitation. Based on the available dual-Doppler data, it is unclear if other CI episodes observed on this day are a result of similar mesoscale processes.

5. Discussion

A variety of short- and long-lived convective cells occurred on 29 November 2018, one short-lived and weak cell occurred in the observing array on 4 December 2018, and a few isolated long-lived cells occurred on 3 July 2015. Estimates of ML CIN in the near-cloud environment immediately preceding CI are similar across each case ($<10\,\text{J kg}^{-1}$; Fig. 14a). Thus, the near-elimination of CIN did not appear to differentiate CI outcome, consistent with conclusions by several past studies (e.g., Rhea 1966; Ziegler and Rasmussen 1998; Markowski and Richardson 2010; Khodayar et al. 2010). These near-cloud soundings are those launched closest to the mesoscale features that trigger CI; thus, the near-elimination of CIN among these soundings may be indicative of the environment that is locally primed for CI by mesoscale moisture convergence and lift (e.g., Ziegler et al. 1997). Investigations of the 15 July 2007 COPS event conclude that moisture advection and forced ascent by mesoscale convergence features and thermally induced orographic flow was required to lift parcels through moderate CIN (Kalthoff et al. 2009; Behrendt et al. 2011; Khodayar et al. 2013). However, in both that case and ours, the full mesoscale environmental heterogeneity may not be ideally observed to differentiate whether mesoscale ascent locally

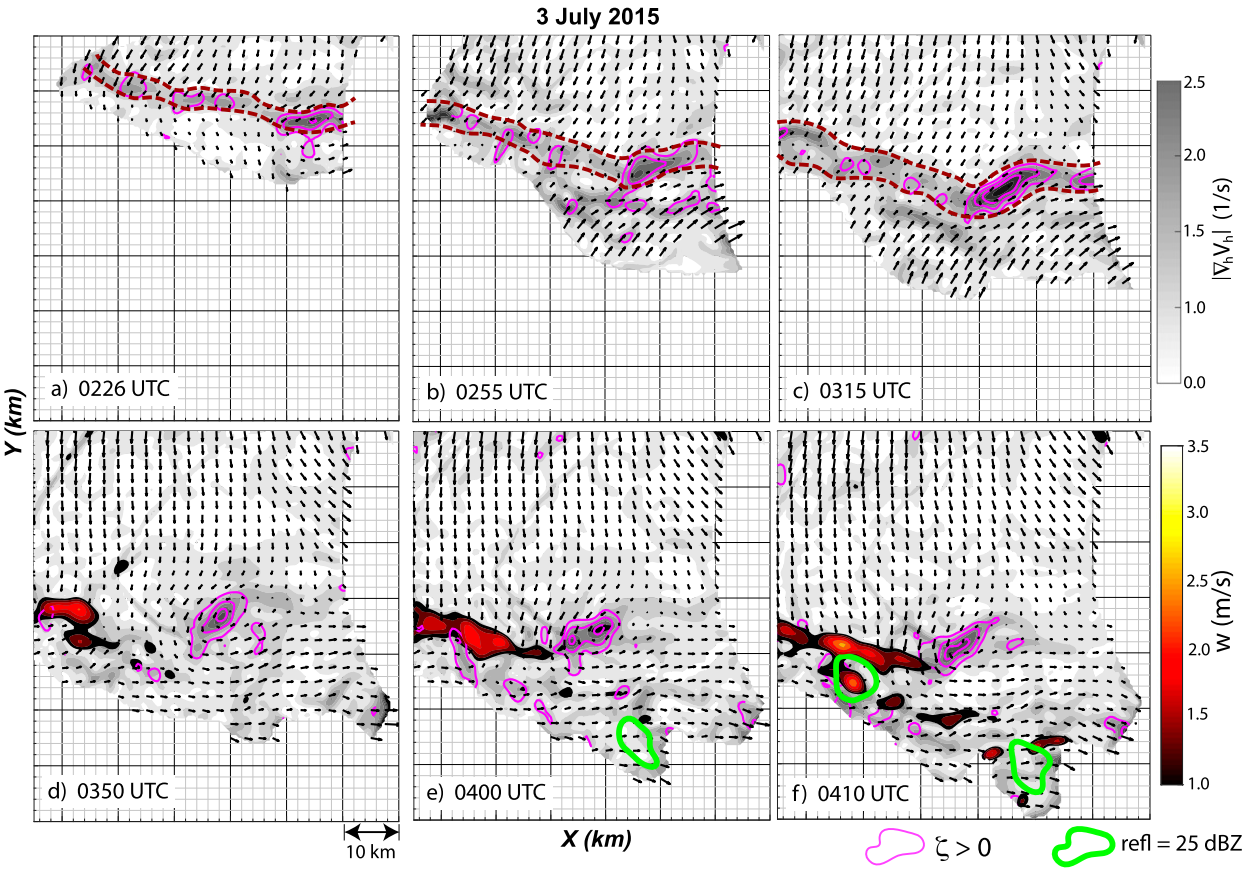

FIG. 13. (a)–(f) Radar reflectivity at $z = 1$ km AGL (25 dBZ; green contour), positive vertical vorticity (purple contours; outermost is 0.001 s^{-1}, incremented by 0.001 s^{-1}), and updraft [red–yellow shading in (d)–(f)] at $z = 1.25$ km AGL, using dual-Doppler wind retrievals between 0226 and 0410 UTC 3 Jul 2015. Horizontal velocity gradient tensor (gray shading) produced using quasi-2D dual-Doppler wind syntheses (as in Fig. 8). Subjective width of the boundary is highlighted with dashed purple contours in (a)–(c).

reduces CIN or simply forces parcels vertically through the CIN layer.

ML CAPE values are also similar across the three cases, spanning from ~600 (4 December) to 680 J kg^{-1} (3 July)[3] when parcel buoyancy is vertically integrated between the LFC and equilibrium level. However, there are differences in the vertical distribution of environmental lapse rates within the column, which are the most (least) stable near and just above the LFC for the 4 December (3 July) case (Fig. 14b). Sustained CI on 3 July and 29 November may be supported by greater instability found lower in the column (e.g., statically neutral layers near ~500 and 585 hPa in the red profile in Fig. 14a) than during 4 December, promoting larger values of buoyancy just above the LFC to help offset buoyancy dilution by entrainment (Houston and Niyogi 2007). It is difficult to generalize the impact of environmental relative humidity on CI outcome, because 4 December and 3 July have similarly dry well-mixed boundary layers, and greater free tropospheric humidity below $z = 5$ km AGL than 29 November (Fig. 14c). Nelson et al. (2021) indicate small variance among relative humidity profiles and deep CAPE measurements observed among a larger sample of sustained and unsustained CI events, suggesting that correlations between humidity profiles and CI outcome in our small sample may not be statistically significant. The height of the boundary layer top is similar to the ML LFC in all three cases (Fig. 14d), suggesting that conditions promoting CBL updrafts to reach the LFC is not a sufficient condition for CI. However, we note that the LFC is sensitive to the resolved details of temperature inversions and moist-adiabatic layers in the lower atmosphere (e.g., the red profile in Fig. 14a).

Some studies suggest that environmental vertical wind shear may inhibit CI due to augmentation of entrainment or adverse pressure gradient forces (e.g., Zhao and Austin 2005; Markowski et al. 2006; Markowski and Richardson 2010; Peters et al. 2019). It is difficult to consistently measure

[3] Limited available parcel trajectory analysis (not shown) suggests that ascent along the wind shift boundary may contain a mixture of air originating from the north and the south. If true, the net ML CIN and CAPE for updraft parcels could lie between 5 and 54 J kg^{-1} and between 351 and 680 J kg^{-1}, respectively.

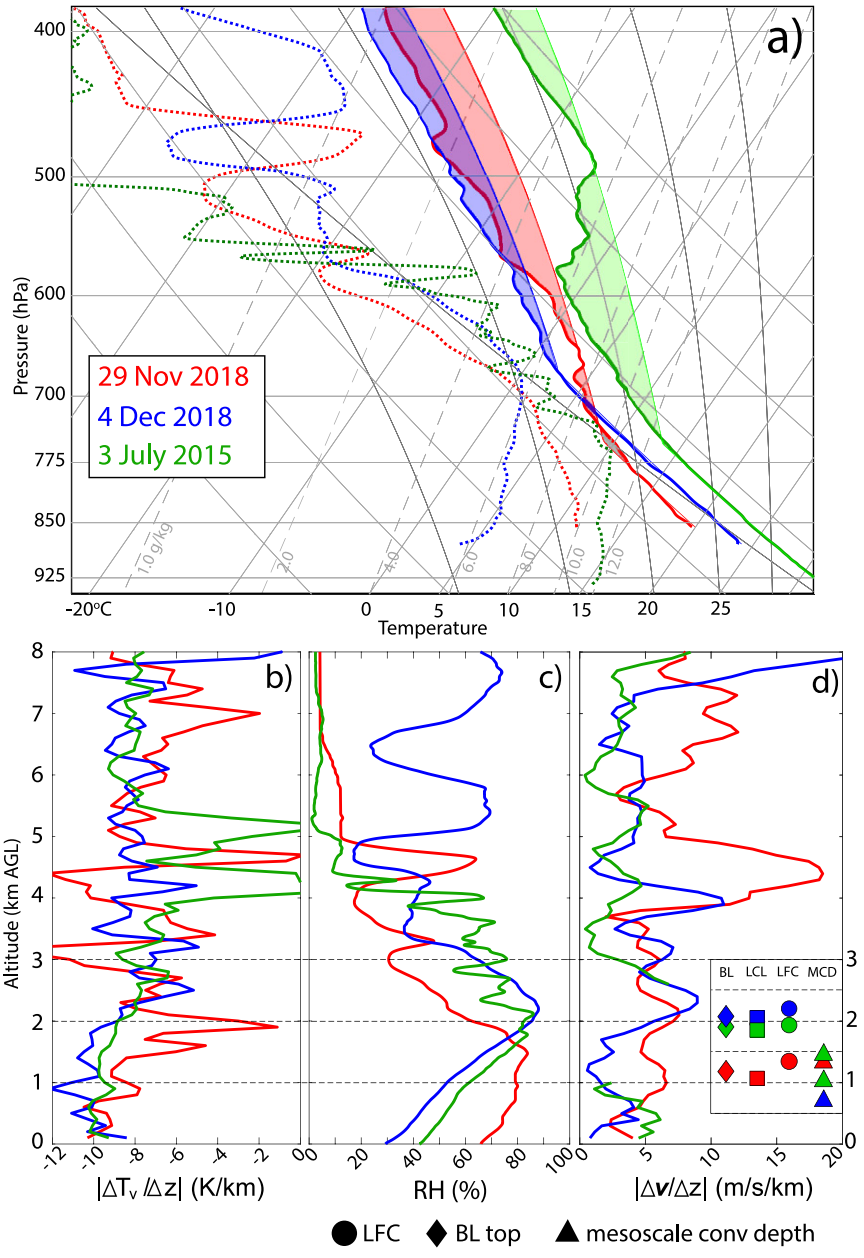

FIG. 14. (a) Skew *T*–log*p* diagrams of radiosonde profiles collected closest in time and space to CI events on 29 Nov (red), 4 Dec (blue), and 3 Jul (green). The 3 Jul profile comprises the combined 0100 UTC AERI and 0300 UTC radiosonde. Layers of positive and negative buoyancy of a ML parcel are shaded for each profile. Vertical profiles of (b) lapse rate of virtual temperature, (c) relative humidity, and (d) vertical wind shear. Estimates of the height of the ML LFC (circles), ML LCL (squares), boundary layer top (diamonds; measured as in Liu and Liang 2010), and dual-Doppler or Lidar estimates of the depth of mesoscale horizontal convergence (triangles) are shown in an offset in (d). Two green triangles indicate the ranges of convergence detected ahead of and along the 3 Jul wind shift, discussed in section 5.

spatiotemporal variation of vertical wind shear with the dual-Doppler data (e.g., Markowski and Richardson 2007) across cases because of differing radar deployment geometry and quality of clear-air returns. Radiosonde-measured shear does not suggest a clear negative correlation with overall daily deep convective potential across the cases because 29 November has the largest vertical wind shear in the free troposphere (Fig. 14d), and sustained CI occurs when shear increases in the 1–3 km AGL layer associated with increased upslope flow (Figs. 5a–f). However, vertical wind shear may pose a more

negative impact on relatively narrow updrafts (Peters et al. 2019); thus, updrafts like those seen during the 4 December case may be more impeded than the wider 29 November updrafts despite weaker background shear.

Mesoscale horizontal variations of metrics relevant to CI (e.g., CAPE, CIN, boundary layer depth, etc.) sometimes varied significantly during the RELAMPAGO-CACTI deployments and were difficult to generalize across each case. CIN was not always minimized over the launch sites located at highest elevation, contrary to observations collected during COPS (Kalthoff et al. 2011). Generally, boundary layer depth did not significantly vary in the 2 h preceding CI (Fig. 5), except on 29 November when it deepened nearest to the location of CI (green sounding in Figs. 5a–c) and at the northernmost sounding site (red sounding in Figs. 5c–e). There is perhaps some indication that the boundary layer is a few hundred meters deeper west of the SDC than east of it on 29 November; though, the opposite is true on 4 December. Otherwise, there are generally subtle variations in boundary layer depth relative to terrain and launch location. This is perhaps similar to Behrendt et al. (2011), except for drastic growth of boundary layer depth that they report at one site in complex terrain. However, certain potentially critical portions of the RELAMPAGO-CACTI domain were not well-observed leading up to CI, such as very near the top of the ridgeline; therefore, it is not possible to definitively compare variations of meteorological metrics across the full terrain profile (e.g., Kalthoff et al. 2011).

The short-lived convection on 4 December dissipates quickly as it travels eastward away from the high terrain. The comparatively well-developed orographic circulations along the terrain on 29 November and wind shift boundary on 3 July appear to allow for more continuous mesoscale lift and CI processes to maintain precipitating updrafts. Thus, the two most robust convection events occurred on the days with the clearest signal of mesoscale convergence, and the longest-lived cells remain in close proximity to it throughout their lifetime.

Subject to the constraints of resolvable spatial scales and coverage of the dual-Doppler analyses on each day, the horizontal widths of these mesoscale convergence regions range between 2 and 8 km (Figs. 5a–e, 8b,c) and are a product of circulations occurring on a variety of scales. On 3 July, a 4-km-wide swath of convergence widens to 6–8 km by the influence of a 5–10-km-wide cyclonic circulation. On 29 November, convergence along the SDC contained $O(1)$-km horizontal structure similar to that within the neighboring boundary layer, indicating that it can be locally enhanced by CBL convection (e.g., Raymond and Wilkening 1980; Demko and Geerts 2010). Manually removing wind data associated with deep precipitating updrafts slightly reduces the magnitudes of meridional-mean convergence and upward motion, especially as CI occurs near the SDC ridgeline after 1630 UTC 29 November (not shown). As a result, it is difficult to unambiguously determine the relative widths of sustained low-level convective updrafts associated with CI and the meridional mean mesoscale convergence region during the 29 November case.

The depths of the mesoscale ascent are difficult to consistently compare across cases because of the variable quality of dual-Doppler wind retrievals and lidar instrument placement relative to CI location and timing. We estimate that mesoscale convergence (updraft) extends from the surface up to approximately 1.25–1.5 (1.5–2.0) km AGL on 29 November and 0.75 km AGL on 4 December. The shallowness of dual-Doppler retrievals because of poor clear air returns aloft on 4 December and 3 July make the vertical extent of updraft unclear. From lidar velocity observations on 3 July (assuming slabular cross frontal flow with time-to-space conversion), we estimate that convergence extends up to ~1.25–1.5 km AGL associated with isolated boundary layer updrafts just ahead of the surface wind shift, and up to ~1 km AGL along it (Fig. 9). Weak updraft is detected ahead of the wind shift up to 1.75 km AGL. Radiosonde measurements are not available within mesoscale ascent regions at the time of CI to analyze the local LFC, but the soundings closest to them suggest that neither convergence nor updraft extends up to the ML LFC in any case (Fig. 14d). From these observations, mesoscale ascent extending up to the ML LFC does not appear to be a *necessary* condition for CI, but likely is beneficial because the days with the estimated deepest convergence yielded the most sustained CI.

Furthermore, subject to the 10–15-min analysis frequency and spatial resolution afforded by the dual-Doppler syntheses, the earliest-detected low-level updrafts associated with the most sustained convection are roughly twice as wide as updrafts associated with nearby CBL turbulence. This comparison may suggest that cloudy updrafts instigated by individual dry thermals ubiquitous to the CBL are insufficiently wide to survive the negative buoyancy dilution effects of entrainment outside of a mesoscale convergence region. Whereas, wider updrafts occurring within regions of subcloud mesoscale forcing and moisture convergence, perhaps initiated by embedded CBL turbulence, are comparatively less susceptible to buoyancy dilution. Furthermore, boundary layer updrafts may be able to saturate more easily within the region of mesoscale forcing owing to locally modified thermodynamic and moisture conditions. This latent heating may add to their potency beyond that governed by subcloud forcing and turbulence structure from CBL dynamics alone; though, it may also have ramifications to reduce thermal width relative to drier updrafts (Morrison et al. 2021).

The distribution of updraft sizes and nearby ambient profiles across cases appears to be consistent with Rousseau-Rizzi et al. (2017). They find that wider low-level updrafts (measured near the LFC), especially occurring within regions of subcloud mesoscale forcing, favor CI more than narrow ones because of larger obtainable positive buoyancy and updraft. Further, the steep ambient lapse rates above the LFC in the 29 November and 3 July cases (Fig. 14) are associated with more robust convection than the 4 December case, possibly consistent with Houston and Niyogi (2007) and Rousseau-Rizzi et al. (2017). It is possible that having relatively wide (and thus, relatively dilution-immune) low-level updrafts is critical for sustained CI processes in environments containing negative vertical moisture gradients at low levels (e.g., the 29 November case; Fig. 6b).

The altitudes of updraft measurements shown in Figs. 11–13 are chosen because they are the highest within the dual-Doppler data volumes containing the most consistent horizontally

continuous coverage. However, updraft width may vary based on its vertical placement relative to a variety of meteorologically relevant depths, such as the LCL, LFC, and boundary layer top (Keene and Lareau 2019; N. Lareau 2021, personal communication). The updrafts located 5–15 km east of the ridgeline on 29 November (collected at z = 1.5 km AGL in Fig. 11) are measured ~0.4 km above the LCL, ~0.15 km above the LFC, and ~0.35 km above the CBL top estimated from the nearby radiosonde (Fig. 14). The cross section of the weakly precipitating cell on 4 December (at z = 1.0 km AGL; Fig. 12b) is measured approximately 1.2 km below the LCL and CBL top and 1.4 km below the LFC. Finally, the developing updraft on 3 July 2015 (at z = 1.25 km AGL; Figs. 13d–f) is measured approximately 0.7 km below the LFC, 0.6 km below the LCL, and 0.6 km below the CBL top. Therefore, our measurement altitudes might comprise an unequal comparison of updraft width and strength across these cases. The controls on updraft width by ambient meteorological conditions are still active areas of research, and some important details of the mesoscale environment (e.g., thermodynamic profiles within the regions of mesoscale ascent) are not consistently captured throughout our observing domains. These, caveats should be considered when comparing our results with other studies.

6. Summary

This study examined rare coordinated radiosonde observations and dual-Doppler radar wind retrievals capturing the initiation of deep moist convection during the RELAMPAGO, CACTI and PECAN field campaigns, permitting a detailed analysis of the environmental controls on the development of early convective updrafts. We focus on two main objectives, examining: (i) the interplay of mesoscale circulations and boundary layer flow convergence with the surrounding thermodynamic conditions that trigger deep convection initiation (CI), and (ii) the evolution of the size and intensity of the earliest detectable low-level precipitating updrafts. We compare three cases in which a variety of deep convective outcomes are observed, from poorly sustained CI processes yielding weak and short-lived cells to better-sustained CI events producing cells lasting a few hours.

Radiosonde measurements best representing the near-cloud environment indicated that CIN was effectively eliminated in all three cases. Low-to-middle tropospheric lapse rates generally were more unstable in the near-cloud environments of sustained CI events than in the poorly sustained events. This resulted in a vertical distribution of CAPE that favored larger updraft buoyancy near the LFC rather than higher in the troposphere, potentially aiding CI processes by offsetting buoyancy dilution from entrainment of environmental air. Of all metrics considered, the depth of the mesoscale lift best differentiated convective outcome, with the most sustained CI processes occurring with the deepest and most prominently observable low-level mesoscale flow convergence.

Observations of updraft thermal sizes and strengths that comprise deep convective clouds are valuable for understanding theoretical formulations of cloud growth, but are extremely limited in the literature. The earliest detectable low-level updrafts associated with sustained, precipitating deep convective cells were 3–5 km in diameter, larger than the typical 1–3-km-wide shallow updraft thermals associated with the surrounding convective boundary layer turbulence. Weak and short-lived precipitating cells lacked similarly large low-level updrafts that were typically indistinguishable from common convective boundary layer turbulence. The size of typical individual convective boundary layer thermals outside of mesoscale convergence zones may limit the potential for CI in overlying clouds because they are too narrow to survive entrainment from the free troposphere. This conclusion is perhaps partly supported by unsustained CI occurring on a day with little or no CIN, a small difference between the LFC height and boundary layer top, but relatively frail mesoscale convergence. Local variations of the mesoscale convergence mechanism triggering CI occurred owing to convective boundary layer turbulence structure, orography, or cyclonic circulations embedded within a surface wind shift boundary. This finding emphasizes the need to properly resolve or parameterize both mesobeta-scale and mesogamma-scale features of triggering mechanisms in numerical regional and climate models.

Although this work provides valuable three-dimensional measurements of low-level updrafts within deep convective clouds in their early stages relative to surrounding convective boundary layer thermals, the precise evolution of updrafts is partly obfuscated by the 10–15-min frequency and confinement of dual-Doppler observations to low levels (often to below 2.0 km AGL). There is still much to be learned about the physical controls on the size of moist updrafts, especially as air ascending in boundary layer thermals interacts with mesoscale lift and the ambient thermodynamic conditions en route to its LFC. Large eddy simulations with realistic terrain that ingest a large quantity of environmental observations may be an ideal tool for investigating these complex cross-scale relationships. Our cursory exploration of boundary layer depth suggests that terrain may aid in the coupling between the convective boundary layer and an elevated mixed layer, more readily generating deep low-level steep lapse rates than at locations over lower terrain. Future planned work involves further investigation of these cases and similar events to examine the evolution of the convective boundary layer relative to topography and surface properties. In addition, we will examine in-cloud microphysical measurements during the growth of congestus that may give a more detailed understanding of the evolution of updraft buoyancy and early precipitation processes associated with CI.

Acknowledgments. This work is funded by the U.S. Department of Energy's Science Biological and Environmental Research as part of the Atmospheric System Research program, and by NSF Grants AGS-1661707, AGS-1541624, and AGS-1661662. Pacific Northwest National Laboratory is operated by Battelle for the U.S. Department of Energy. Radar data were translated and edited using NCAR's RadX and Solo software. Thank you to David Dowell for writing core radar gridding and dual-Doppler wind synthesis software (OPAWS). Visible satellite images were produced using the University of Wisconsin–

Madison Space Science and Engineering Center's McIDAS-V software. Topographic data for Argentina was acquired at http://viewfinderpanoramas.org/dem3.html. This work benefited from helpful discussions with Stephen Nesbitt, Karen Kosiba, Joseph Hardin, Zhe Feng, Paloma Borque, Russ Schumacher, Jeff Trapp, Lynn McMurdie, Jim Wilson, Neil Lareau, Daniel Kirshbaum, Tammy Weckwerth, and three anonymous reviewers. This work was aided by an undergraduate research assistant at the University of Colorado, Thomas Jarman.

Data availability statement. Data utilized are available on NCAR's Earth Observing Laboratory and ARM's Data Discovery catalogs.

REFERENCES

Alexander, L. S., D. M. Sills, and P. A. Taylor, 2018: Initiation of convective storms at low-level mesoscale boundaries in southwestern Ontario. *Wea. Forecasting*, **33**, 583–598, https://doi.org/10.1175/WAF-D-17-0086.1.

Arnott, N. R., Y. P. Richardson, J. M. Wurman, and E. M. Rasmussen, 2006: Relationship between a weakening cold front, misocyclones, and cloud development on 10 June 2002 during IHOP. *Mon. Wea. Rev.*, **134**, 311–335, https://doi.org/10.1175/MWR3065.1.

Atkins, N. T., R. M. Wakimoto, and T. M. Weckwerth, 1995: Observations of the sea-breeze front during CaPE. Part II: Dual-Doppler and aircraft analysis. *Mon. Wea. Rev.*, **123**, 944–969, https://doi.org/10.1175/1520-0493(1995)123<0944:OOTSBF>2.0.CO;2.

ARM user facility, 2018: Minnis Cloud Products Using VISST Algorithm (VISSTGRIDG16V4MINNIS) (1 October 2018–30 April 2019). ARM Mobile Facility (COR) External Data from Cordoba, Argentina (CACTI) (×1), ARM Data Center, accessed 21 February 2020, https://www.arm.gov/capabilities/vaps/visst/xds.

Banta, R. M., 1984: Daytime boundary-layer evolution over mountainous terrain. Part 1: Observations of the dry circulations. *Mon. Wea. Rev.*, **112**, 340–356, https://doi.org/10.1175/1520-0493(1984)112<0340:DBLEOM>2.0.CO;2.

——, 1986: Daytime boundary-layer evolution over mountainous terrain. Part 2: Numerical studies of upslope flow duration. *Mon. Wea. Rev.*, **114**, 1112–1130, https://doi.org/10.1175/1520-0493(1986)114<1112:DBLEOM>2.0.CO;2.

Barnes, S. L., 1964: A technique for maximizing details in numerical weather map analysis. *J. Appl. Meteor.*, **3**, 396–409, https://doi.org/10.1175/1520-0450(1964)003<0396:ATFMDI>2.0.CO;2.

Behrendt, A., and Coauthors, 2011: Observation of convection initiation processes with a suite of state-of-the-art research instruments during COPS IOP 8b. *Quart. J. Roy. Meteor. Soc.*, **137**, 81–100, https://doi.org/10.1002/qj.758.

Bharadwaj, N., J. Hardin, B. Isom, I. Lindenmaier, A. Matthews, and D. Nelson, 2018: C-Band Scanning ARM Precipitation Radar (CSAPR2CFRPPI). Atmospheric Radiation Measurement (ARM) user facility, September 23, 2018. Accessed 1 September 2019, https://doi.org/10.5439/1482633.

Bretherton, C. S., J. R. McCaa, and H. Grenier, 2004: A new parameterization for shallow cumulus convection and its application to marine subtropical cloud-topped boundary layers. Part I: Description and 1D results. *Mon. Wea. Rev.*, **132**, 864–882, https://doi.org/10.1175/1520-0493(2004)132<0864:ANPFSC>2.0.CO;2.

Browning, K., and Coauthors, 2007: The Convective Storm Initiation Project. *Bull. Amer. Meteor. Soc.*, **88**, 1939–1956, https://doi.org/10.1175/BAMS-88-12-1939.

Bryan, G. H., J. C. Wyngaard, and J. M. Fritsch, 2003: Resolution requirements for the simulation of deep moist convection. *Mon. Wea. Rev.*, **131**, 2394–2416, https://doi.org/10.1175/1520-0493(2003)131<2394:RRFTSO>2.0.CO;2.

Buban, M. S., C. L. Ziegler, E. R. Mansell, and Y. P. Richardson, 2012: Simulation of dryline misovortex dynamics and cumulus formation. *Mon. Wea. Rev.*, **140**, 3525–3551, https://doi.org/10.1175/MWR-D-11-00189.1.

Chikira, M., and M. Sugiyama, 2010: A cumulus parameterization with state dependent entrainment rate. Part I: Description and sensitivity to temperature and humidity profiles. *J. Atmos. Sci.*, **67**, 2171–2193, https://doi.org/10.1175/2010JAS3316.1.

Clark, R., 2015a: FP3 Millersville University Micropulse Lidar (MPL) Imagery, version 1.0. UCAR/NCAR–Earth Observing Laboratory, accessed 1 August 2018, https://doi.org/10.5065/D6XW4GVS.

——, 2015b: FP3 Millersville University Surface Meteorology and Radiation Data, version 1.0. UCAR/NCAR–Earth Observing Laboratory, accessed 4 February 2021, https://doi.org/10.5065/D6CV4FTM.

——, 2016: FP3 Ellis, KS Radiosonde Data, version 2.0. UCAR/NCAR–Earth Observing Laboratory, accessed 1 August 2018, https://doi.org/10.5065/D6GM85DZ.

Craven, J. P., R. E. Jewell, and H. E. Brooks, 2002: Comparison between observed convective cloud-base heights and lifting condensation level for two different lifted parcels. *Wea. Forecasting*, **17**, 885–890, https://doi.org/10.1175/1520-0434(2002)017<0885:CBOCCB>2.0.CO;2.

Damiani, R., and Coauthors, 2008: The cumulus, photogrammetric, in-situ, and Doppler observations experiment of 2006. *Bull. Amer. Meteor. Soc.*, **89**, 57–74, https://doi.org/10.1175/BAMS-89-1-57.

de Rooy, W. C., and Coauthors, 2013: Entrainment and detrainment in cumulus convection: An overview. *Quart. J. Roy. Meteor. Soc.*, **139**, 1–19, https://doi.org/10.1002/qj.1959.

Demko, J. C., and B. Geerts, 2010: A numerical study of the evolving convective boundary layer and orographic circulation around the Santa Catalina Mountains in Arizona. Part I: Circulation without deep convection. *Mon. Wea. Rev.*, **138**, 1902–1922, https://doi.org/10.1175/2009MWR3098.1.

——, ——, Q. Miao, and J. A. Zehnder, 2009: Boundary layer energy transport and cumulus development over a heated mountain: An observational study. *Mon. Wea. Rev.*, **137**, 447–468, https://doi.org/10.1175/2008MWR2467.1.

Derbyshire, S. H., A. V. Maidens, S. F. Milton, R. A. Stratton, and M. R. Willett, 2011: Adaptive detrainment in a convective parameterization. *Quart. J. Roy. Meteor. Soc.*, **137**, 1856–1871, https://doi.org/10.1002/qj.875.

Dowell, D. C., and A. Shapiro, 2003: Stability of an iterative dual-Doppler wind synthesis in Cartesian coordinates. *J. Atmos. Oceanic Technol.*, **20**, 1552–1559, https://doi.org/10.1175/1520-0426(2003)020<1552:SOAIDW>2.0.CO;2.

Garcia-Carreras, L., D. J. Parker, and J. H. Marsham, 2011: What is the mechanism for the modification of convective cloud distributions by land surface–induced flows? *J. Atmos. Sci.*, **68**, 619–634, https://doi.org/10.1175/2010JAS3604.1.

Geerts, B., and Coauthors, 2017: The 2015 Plains Elevated Convection At Night Field Project. *Bull. Amer. Meteor. Soc.*, **98**, 767–786, https://doi.org/10.1175/BAMS-D-15-00257.1.

Hirt, M., G. C. Craig, S. A. K. Schäfer, J. Savre, and R. Heinze, 2020: Cold-pool-driven convective initiation: Using causal graph analysis to determine what convection-permitting models are missing. *Quart. J. Roy. Meteor. Soc.*, **146**, 2205–2227, https://doi.org/10.1002/qj.3788.

Holdridge, D., J. Kyrouac, and E. Keeler, 2018: Balloon-Borne Sounding System (SONDEWNPN). Atmospheric Radiation Measurement (ARM) user facility, September 27, 2018. Accessed 1 September 2019, https://doi.org/10.5439/1021460.

Honomichl, S., A. Detwiler, and P. Smith, 2013: Observed hazards to aircraft in deep summertime convective clouds from 4-7 km. *J. Aircr.*, **50**, 926–935, https://doi.org/10.2514/1.C032057.

Houston, A. L., and D. Niyogi, 2007: The sensitivity of convective initiation to the lapse rate of the active cloud-bearing layer. *Mon. Wea. Rev.*, **135**, 3013–3032, https://doi.org/10.1175/MWR3449.1.

Huang, H.-Y., and S. A. Margulis, 2013: Impact of soil moisture heterogeneity length scale and gradients on daytime coupled land-cloudy boundary layer interactions. *Hydrol. Processes*, **27**, 1988–2003, https://doi.org/10.1002/hyp.9351.

Kain, J. S., 2004: The Kain–Fritsch convective parameterization: An update. *J. Appl. Meteor.*, **43**, 170–181, https://doi.org/10.1175/1520-0450(2004)043<0170:TKCPAU>2.0.CO;2.

——, and J. M. Fritsch, 1990: A one-dimensional entraining/detraining plume model and its application in convective parameterization. *J. Atmos. Sci.*, **47**, 2784–2802, https://doi.org/10.1175/1520-0469(1990)047<2784:AODEPM>2.0.CO;2.

Kalthoff, N., and Coauthors, 2009: The impact of convergence zones on the initiation of deep convection: A case study from COPS. *Atmos. Res.*, **93**, 680–694, https://doi.org/10.1016/j.atmosres.2009.02.010.

——, and Coauthors, 2011: The dependence of convection-related parameters on surface and boundary-layer conditions over complex terrain. *Quart. J. Roy. Meteor. Soc.*, **137**, 70–80, https://doi.org/10.1002/qj.686.

Kang, S., and G. H. Bryan, 2011: A large-eddy simulation study of moist convection initiation over heterogeneous surface fluxes. *Mon. Wea. Rev.*, **139**, 2901–2917, https://doi.org/10.1175/MWR-D-10-05037.1.

Keene, C., and N. Lareau, 2019: The observed variation of updrafts with height in the cumulus topped boundary layer. *2019 Fall Meeting*, San Francisco, CA, Amer. Geophysical Union, Abstract A41L-2745, https://agu-do03.confex.com/agu/fm19/meetingapp.cgi/Paper/631586.

Khodayar, S., N. Kalthoff, J. Wickert, U. Corsmeier, C. Morcrette, and C. Kottmeier, 2010: The increase of spatial data resolution for the detection of the initiation of convection: A case study from CSIP. *Meteor. Z.*, **19**, 179–198, https://doi.org/10.1127/0941-2948/2010/0439.

——, ——, ——, Ch. Kottmeier, and M. Dorninger, 2013: High-resolution representation of the mechanisms responsible for the initiation of isolated thunderstorms over flat and complex terrains: Analysis of CSIP and COPS cases. *Meteor. Atmos. Phys.*, **119**, 109–124, https://doi.org/10.1007/s00703-012-0232-6.

Kim, D., and I.-S. Kang, 2011: A bulk mass flux convection scheme for a climate model: Description and moisture sensitivity. *Climate Dyn.*, **38**, 411–429, https://doi.org/10.1007/s00382-010-0972-2.

Kingsmill, D. E., 1995: Convection initiation associated with a sea-breeze front, a gust front, and their collision. *Mon. Wea. Rev.*, **123**, 2913–2933, https://doi.org/10.1175/1520-0493(1995)123<2913:CIAWAS>2.0.CO;2.

Kirshbaum, D. J., 2011: Cloud-resolving simulations of deep convection over a heated mountain. *J. Atmos. Sci.*, **68**, 361–378, https://doi.org/10.1175/2010JAS3642.1.

——, 2013: On thermally forced circulations over heated terrain. *J. Atmos. Sci.*, **70**, 1690–1709, https://doi.org/10.1175/JAS-D-12-0199.1.

——, B. Adler, N. Kalthoff, C. Barthlott, and S. Serafin, 2018: Moist orographic convection: Physical mechanisms and links to surface-exchange processes. *Atmosphere*, **9**, 80, https://doi.org/10.3390/atmos9030080.

Koch, S. E., M. DesJardins, and P. J. Kocin, 1983: An interactive Barnes objective map analysis scheme for use with satellite and conventional data. *J. Climate Appl. Meteor.*, **22**, 1487–1503, https://doi.org/10.1175/1520-0450(1983)022<1487:AIBOMA>2.0.CO;2.

Kottmeier, C., and Coauthors, 2008: Mechanisms initiating deep convection over complex terrain during COPS. *Meteor. Z.*, **17**, 931–948, https://doi.org/10.1127/0941-2948/2008/0348.

Kyrouac, J., and D. Holdridge, 2018: Surface Meteorological Instrumentation (MET). Atmospheric Radiation Measurement (ARM) user facility, accessed 1 September 2019, https://doi.org/10.5439/1025220.

Lee, B. D., and R. Wilhelmson, 1997: The numerical simulation of nonsupercell tornadogenesis. Part I: Initiation and evolution of pretornadic misocyclone circulations along a dry outflow boundary. *J. Atmos. Sci.*, **54**, 32–60, https://doi.org/10.1175/1520-0469(1997)054<0032:TNSONS>2.0.CO;2.

——, C. A. Finley, and R. B. Wilhelmson, 2000: Simulating deep convection initiation by misocyclones. Preprints, *20th Conf. on Severe Local Storms*, Orlando, FL, Amer. Meteor. Soc., 70–73.

Lima, M. A., and J. W. Wilson, 2008: Convective storm initiation in a moist tropical environment. *Mon. Wea. Rev.*, **136**, 1847–1864, https://doi.org/10.1175/2007MWR2279.1.

Liu, S., and X. Z. Liang, 2010: Observed diurnal cycle climatology of planetary boundary layer height. *J. Climate*, **23**, 5790–5809, https://doi.org/10.1175/2010JCLI3552.1.

Majcen, M., P. Markowski, Y. Richardson, D. Dowell, and J. Wurman, 2008: Multipass objective analyses of Doppler radar data. *J. Atmos. Oceanic Technol.*, **25**, 1845–1858, https://doi.org/10.1175/2008JTECHA1089.1.

Markowski, P., and Y. Richardson, 2007: Observations of vertical wind shear heterogeneity in convective boundary layers. *Mon. Wea. Rev.*, **135**, 843–861, https://doi.org/10.1175/MWR3334.1.

——, and ——, 2010: Mesoscale Meteorology in Midlatitudes. Wiley-Blackwell, 407 pp.

——, C. Hannon, and E. Rasmussen, 2006: Observations of convection initiation "failure" from the 12 June 2002 IHOP deployment. *Mon. Wea. Rev.*, **134**, 375–405, https://doi.org/10.1175/MWR3059.1.

Marquis, J. N., Y. P. Richardson, and J. M. Wurman, 2007: Kinematic observations of misocyclones along boundaries during IHOP. *Mon. Wea. Rev.*, **135**, 1749–1768, https://doi.org/10.1175/MWR3367.1.

McCoy, R., S. Xie, Y. Zhang, and D. Cook, 2018: Quality Controlled Eddy Correlation Flux Measurement (30QCECOR). Atmospheric Radiation Measurement (ARM) user facility (September 23). Accessed 15 February 2021, https://doi.org/10.5439/1097546.

Miller, R. L., C. L. Ziegler, and M. I. Biggerstaff, 2020: Seven-Doppler radar and in situ analysis of the 25–26 June 2015 Kansas MCS during PECAN. *Mon. Wea. Rev.*, **148**, 211–240, https://doi.org/10.1175/MWR-D-19-0151.1.

Morrison, H., 2016: Impacts of updraft size and dimensionality on the perturbation pressure and vertical velocity in cumulus

convection. Part II: Comparison of theoretical and numerical solutions. *J. Atmos. Sci.*, **73**, 1455–1480, https://doi.org/10.1175/JAS-D-15-0041.1.

——, 2017: An analytic description of the structure and evolution of growing deep cumulus updrafts. *J. Atmos. Sci.*, **74**, 809–834, https://doi.org/10.1175/JAS-D-16-0234.1.

——, J. M. Peters, and S. C. Sherwood, 2021: Comparing growth rates of simulated moist and dry convective thermals. *J. Atmos. Sci.*, **78**, 797–816, https://doi.org/10.1175/JAS-D-20-0166.1.

Moser, D. H., and S. Lasher-Trapp, 2017: The influence of successive thermals on entrainment and dilution in a simulated cumulus congestus. *J. Atmos. Sci.*, **74**, 375–392, https://doi.org/10.1175/JAS-D-16-0144.1.

Mulholland, J. P., S. W. Nesbitt, R. J. Trapp, and J. M. Peters, 2020: The influence of terrain on the convective environment and associated convective morphology from an idealized modeling prospective. *J. Atmos. Sci.*, **77**, 3929–3949, https://doi.org/10.1175/JAS-D-19-0190.1.

Musil, D. J., S. A. Christopher, R. A. Deola, and P. L. Smith, 1991: Some interior observations of Southeastern Montana hailstorms. *J. Appl. Meteor.*, **30**, 1596–1612, https://doi.org/10.1175/1520-0450(1991)030<1596:SIOOSM>2.0.CO;2.

Nelson, T. C., J. Marquis, A. Varble, and K. Friedrich, 2021: Radiosonde observations of environments supporting deep moist convection initiation during RELAMPAGO-CACTI. *Mon. Wea. Rev.*, **149**, 289–309, https://doi.org/10.1175/MWR-D-20-0148.1.

Nesbitt, S. W., and Coauthors, 2021: A storm safari in subtropical South America: Project RELAMPAGO. *Bull. Amer. Meteor. Soc.*, https://doi.org/10.1175/BAMS-D-20-0029.1,in press.

Pauley, P. M., and X. Wu, 1990: The theoretical, discrete, and actual response of the Barnes objective analysis scheme for one- and two-dimensional fields. *Mon. Wea. Rev.*, **118**, 1145–1164, https://doi.org/10.1175/1520-0493(1990)118<1145:TTDAAR>2.0.CO;2.

Peckham, S. E., R. B. Wilhelmson, L. J. Wicker, and C. L. Ziegler, 2004: Numerical simulation of the interaction between the dryline and horizontal convective rolls. *Mon. Wea. Rev.*, **132**, 1792–1812, https://doi.org/10.1175/1520-0493(2004)132<1792:NSOTIB>2.0.CO;2.

Peters, J. M., W. Hannah, and H. Morrison, 2019: The influence of vertical wind shear on moist thermals. *J. Atmos. Sci.*, **76**, 1645–1659, https://doi.org/10.1175/JAS-D-18-0296.1.

Rasmussen, K. L., and R. A. Houze Jr., 2016: Convective initiation near the Andes in subtropical South America. *Mon. Wea. Rev.*, **144**, 2351–2374, https://doi.org/10.1175/MWR-D-15-0058.1.

Raymond, D., and M. Wilkening, 1980: Mountain-induced convection under fair weather conditions. *J. Atmos. Sci.*, **37**, 2693–2706, https://doi.org/10.1175/1520-0469(1980)037<2693:MICUFW>2.0.CO;2.

Rhea, J. O., 1966: A study of thunderstorm formation along drylines. *J. Appl. Meteor.*, **5**, 58–63, https://doi.org/10.1175/1520-0450(1966)005<0058:ASOTFA>2.0.CO;2.

Rieck, M., C. Hohenegger, and C. C. van Heerwaarden, 2014: The influence of land surface heterogeneities on cloud size development. *Mon. Wea. Rev.*, **142**, 3830–3846, https://doi.org/10.1175/MWR-D-13-00354.1.

Rosenfeld, D., W. L. Woodley, T. W. Krauss, and V. Makitov, 2006: Aircraft microphysical documentation from cloud base to anvils of hailstorm feeder clouds in Argentina. *J. Appl. Meteor. Climatol.*, **45**, 1261–1281, https://doi.org/10.1175/JAM2403.1.

Rousseau-Rizzi, R., D. J. Kirshbaum, and M. K. Yau, 2017: Initiation of deep convection over an idealized mesoscale convergence line. *J. Atmos. Sci.*, **74**, 835–853, https://doi.org/10.1175/JAS-D-16-0221.1.

Schumacher, R., 2019: CSU Mobile Radiosonde Data, version 1.0. UCAR/NCAR–Earth Observing Laboratory, accessed 1 September 2019, https://doi.org/10.26023/3QGG-JQKS-AF0G.

Stonitsch, J. R., and P. M. Markowski, 2007: Unusually long duration, multiple-Doppler radar observations of a front in a convective boundary layer. *Mon. Wea. Rev.*, **135**, 93–117, https://doi.org/10.1175/MWR3261.1.

Tiedtke, M., 1989: A comprehensive mass flux scheme for cumulus parameterization in large-scale models. *Mon. Wea. Rev.*, **117**, 1779–1800, https://doi.org/10.1175/1520-0493(1989)117<1779:ACMFSF>2.0.CO;2.

Trapp, R. J., and C. A. Doswell III, 2000: Radar data objective analysis. *J. Atmos. Oceanic Technol.*, **17**, 105–120, https://doi.org/10.1175/1520-0426(2000)017<0105:RDOA>2.0.CO;2.

Turner, D. 2016: FP3 AERIoe Thermodynamic Profile Retrieval Data, version 2.0. UCAR/NCAR–Earth Observing Laboratory, accessed 1 September 2019, https://doi.org/10.5065/D6Z31WV0.

UCAR/NCAR–Earth Observing Laboratory, 2016: S-Pol Radar moments data in cfRadial format, version 2.0. UCAR/NCAR–Earth Observing Laboratory, accessed 1 September 2019, https://doi.org/10.5065/D6PN93VJ.

——, 2019: GOES-16 Advanced Baseline Imager (ABI) Mesoscale Sector Data, version 1.0. UCAR/NCAR–Earth Observing Laboratory, accessed 22 February 2021, https://doi.org/10.26023/QRRG-E5BH-JT0D.

Varble, A., and Coauthors, 2014: Evaluation of cloud-resolving and limited area model intercomparison simulations using TWP-ICE observations: 1. Deep convective updraft properties. *J. Geophys. Res. Atmos.*, **119**, 13891–13918, https://doi.org/10.1002/2013JD021371.

——, and Coauthors, 2021: Utilizing a storm-generating hotspot to study convective cloud transitions: The CACTI experiment. *Bull. Amer. Meteor. Soc.*, https://doi.org/10.1175/BAMS-D-20-0030.1, in press.

——, H. Morrison, and E. Zipser, 2020: Effects of under-resolved convective dynamics on the evolution of a squall line. *Mon. Wea. Rev.*, **148**, 289–311, https://doi.org/10.1175/MWR-D-19-0187.1.

Wagner, T., and H. F. Graf, 2010: An ensemble cumulus convection parameterization with explicit cloud treatment. *J. Atmos. Sci.*, **67**, 3854–3869, https://doi.org/10.1175/2010JAS3485.1.

——, D. Turner, and R. Newsom, 2016a: MP3 University of Wisconsin SPARC Doppler Lidar VAD Wind Data, version 2.0. UCAR/NCAR–Earth Observing Laboratory, accessed 19 July 2018, https://doi.org/10.5065/D6V9869B.

——, ——, and ——, 2016b: MP3 University of Wisconsin SPARC Doppler Lidar Zenith Pointing Data, version 2.0. UCAR/NCAR–Earth Observing Laboratory, accessed 19 July 2018, https://doi.org/10.5065/D6QJ7FJ5.

Waugh, S., and S. E. Fredrickson, 2010: An improved aspirated temperature system for mobile meteorological observations, especially in severe weather. *25th Conf. on Severe Local Storms,* Denver, CO, Amer. Meteor. Soc., P5.2, https://ams.confex.com/ams/25SLS/webprogram/Paper176205.html.

Weckwerth, T. M., and R. M. Wakimoto, 1992: The initiation and organization of convective cells atop a cold-air outflow boundary. *Mon. Wea. Rev.*, **120**, 2169–2187, https://doi.org/10.1175/1520-0493(1992)120<2169:TIAOOC>2.0.CO;2.

——, J. W. Wilson, and R. M. Wakimoto, 1996: Thermodynamic variability within the convective boundary layer due to horizontal convective rolls. *Mon. Wea. Rev.*, **124**, 769–784, https://doi.org/10.1175/1520-0493(1996)124<0769:TVWTCB>2.0.CO;2.

——, and Coauthors, 2004: An overview of the International H_2O Project (IHOP) and some preliminary highlights. *Bull. Amer. Meteor. Soc.*, **85**, 253–278, https://doi.org/10.1175/BAMS-85-2-253.

——, J. Hanesiak, J. W. Wilson, S. B. Trier, S. K. Degelia, W. A. Gallus, R. D. Roberts, and X. Wang, 2019: Nocturnal convection initiation during PECAN 2015. *Bull. Amer. Meteor. Soc.*, **100**, 2223–2239, https://doi.org/10.1175/BAMS-D-18-0299.1.

Wilson, J. W., and W. E. Schreiber, 1986: Initiation of convective storms at radar-observed boundary-layer convergence lines. *Mon. Wea. Rev.*, **114**, 2516–2536, https://doi.org/10.1175/1520-0493(1986)114<2516:IOCSAR>2.0.CO;2.

——, and D. L. Megenhardt, 1997: Thunderstorm initiation, organization, and lifetime associated with Florida boundary layer convergence zones. *Mon. Wea. Rev.*, **125**, 1507–1525, https://doi.org/10.1175/1520-0493(1997)125<1507:TIOALA>2.0.CO;2.

——, and R. Roberts, 2006: Summary of convective storm initiation and evolution during IHOP: Observational and modeling perspective. *Mon. Wea. Rev.*, **134**, 23–47, https://doi.org/10.1175/MWR3069.1.

——, J. A. Moore, G. B. Foote, B. Martner, A. R. Rodi, T. Uttal, and J. M. Wilczak, 1988: Convection Initiation and Downburst Experiment (CINDE). *Bull. Amer. Meteor. Soc.*, **69**, 1328–1347, https://doi.org/10.1175/1520-0477(1988)069<1328:CIADE>2.0.CO;2.

——, G. B. Foote, N. A. Crook, J. C. Fankhauser, C. G. Wade, J. D. Tuttle, and C. K. Mueller, 1992: The role of boundary-layer convergence zones and horizontal rolls in the initiation of thunderstorms: A case study. *Mon. Wea. Rev.*, **120**, 1785–1815, https://doi.org/10.1175/1520-0493(1992)120<1785:TROBLC>2.0.CO;2.

Wulfmeyer, V., and Coauthors, 2008: The Convective and Orographically Induced Precipitation Study: A research and development project of the World Weather Research Program for improving quantitative precipitation forecasting in low-mountain regions. *Bull. Amer. Meteor. Soc.*, **89**, 1469–1506, https://doi.org/10.1175/1520-0477-89.10.1469.1.

Wurman, J., and K. Kosiba, 2018a: FARM-data-PECAN (version 1): Doppler on Wheels data set. Center for Severe Weather Research, accessed 1 July 2017, https://doi.org/10.48514/PASW-DE36.

——, and ——, 2018b: FARM-data-PECAN (version 1): Scout mobile mesonet data sets. Center for Severe Weather Research, accessed 1 July 2018, https://doi.org/10.48514/PASW-DE36.

——, and ——, 2021a: FARM-data-RELAMPAGO (version 1): Radiosonde data set. Center for Severe Weather Research, accessed 1 May 2019, https://doi.org/10.48514/NK1P-7J11.

——, and ——, 2021b: FARM-data-RELAMPAGO (version 1): Doppler on Wheels data set. Center for Severe Weather Research, accessed 1 March 2019, https://doi.org/10.48514/NK1P-7J11.

——, and ——, 2021c: FARM-data-RELAMPAGO (version 1): Pod surface station data set. Center for Severe Weather Research, accessed 1 May 2019, https://doi.org/10.48514/NK1P-7J11.

——, and ——, 2021d: FARM-data-RELAMPAGO (version 1): Mobile mesonet surface station data set. Center for Severe Weather Research, accessed 1 May 2019, https://doi.org/10.48514/NK1P-7J11.

Xue, M., and W. J. Martin, 2006: A high-resolution modeling study of the 24 May 2002 dryline case during IHOP. Part II: Horizontal convective rolls and convective initiation. *Mon. Wea. Rev.*, **134**, 172–191, https://doi.org/10.1175/MWR3072.1.

Yano, J., F. Guichard, J. Lafore, J. Redelsperger, and P. Bechtold, 2004: Estimations of mass fluxes for cumulus parameterizations from high-resolution spatial data. *J. Atmos. Sci.*, **61**, 829–842, https://doi.org/10.1175/1520-0469(2004)061<0829:EOMFFC>2.0.CO;2.

Zhao, M., and P. H. Austin, 2005: Life cycle of numerically simulated shallow cumulus clouds. Part II: Mixing dynamics. *J. Atmos. Sci.*, **62**, 1291–1310, https://doi.org/10.1175/JAS3415.1.

Ziegler, C. L., and E. N. Rasmussen, 1998: The initiation of moist convection at the dryline: Forecasting issues from a case study perspective. *Wea. Forecasting*, **13**, 1106–1131, https://doi.org/10.1175/1520-0434(1998)013<1106:TIOMCA>2.0.CO;2.

——, T. J. Lee, and R. A. Pielke, 1997: Convective initiation at the dryline: A modeling study. *Mon. Wea. Rev.*, **125**, 1001–1026, https://doi.org/10.1175/1520-0493(1997)125<1001:CIATDA>2.0.CO;2.

——, E. N. Rasmussen, M. S. Buban, Y. P. Richardson, L. J. Miller, and R. M. Rabin, 2007: The ''Triple Point'' on 24 May 2002 during IHOP. Part II: Ground-radar and in situ boundary layer analysis of cumulus development and convection initiation. *Mon. Wea. Rev.*, **135**, 2443–2472, https://doi.org/10.1175/MWR3411.1.